Numerical Modelling of a Pulsed Waterjet Using the Discontinuous-Galerkin-Hancock Method

Ibrahim Rizk

Thesis submitted to the University of Ottawa
in partial Fulfillment of the requirements for the
Masters of Applied Science

Graduate Department of Mechanical Engineering
University of Ottawa

Numerical Modelling of a Pulsed Waterjet Using the Discontinuous-Galerkin-Hancock Method

Ibrahim Rizk
Masters of Applied Science
Graduate Department of Mechanical Engineering
University of Ottawa
2024

Abstract

A high-pressure pulsed waterjet actuated by a high-frequency oscillating probe is studied numerically. A compressible hyperbolic flow model is derived from the Saurel model [27] for the numerical simulation of multiphase flows with phase transition and uses the discontinuous-Galerkin-Hancock method. The model uses the mixture Euler equations and the Noble-Abel stiffened-gas equation of state as a thermodynamic closure. The phase change is driven by a difference in Gibbs free energies in the phases, leading to a stiff relaxation term representing the cavitation rate. Each phase is compressible and evolves, sharing a single pressure, velocity, and temperature. Numerical studies were carried out to analyse cavitating flows in venturi geometries, which agree with experimental data to illustrate the flow model's applicability.

This thesis presents a comprehensive study of the pulsed waterjet with and without the oscillating probe. In the first scenario, the pulsed waterjet is without the oscillating probe. The nozzle produces a jet of water with a maximum velocity of 440 m/s. When the jet collides with the wall, a pronounced water hammer effect produces a peak pressure of 82.6 MPa. The jet exhibits improved performance in the second scenario with the oscillating probe. The flow of the jet of water changes physically, producing mushroom-like packets due to alternating high and low-pressure waves induced by the probe. The maximum velocity is also faster at 470 m/s. When the jet collides with the wall, the effect of the water hammer produces a maximum pressure of 110.0 MPa, which is 23 % higher than the standard jet. The minimum pressure produced is 60.0 MPa. The numerical simu-

lations found no cavitation produced by the water jet outside the nozzle. These predicted results offer insight into the complex behaviours of the pulsed waterjet.

To my family

Acknowledgements

I would like to thank Dr. James McDonald, VLN, and my family. I would also like to thank Compute Canada for allowing me to use their supercomputers.

Contents

List of Tables

List of Figures

Chapter 1

Introduction

Surface engineering is a subset of mechanical engineering that is concerned with the fabrication of functional coatings. A functional coating is a surface coating that provides a specific function or adds a desired property to a surface. It is extensively used in the aerospace, automotive, power generation, biomedical and petrochemical sectors to extend components' useful life and performance. Functional coatings require surface preparation to expel surface contaminants and impart physical anchor points that promote the mechanical adhesion of a coating to a substrate. VLN Advanced Technologies manufactures water jets for surface preparation. VLN is exploring the possible modification of its Pulsed Waterjet (PWJ) for green surface preparation. VLN is interested in understanding the underlying process physics to allow the optimisation of the PWJ for surface preparation.

The main goal of this thesis is to elucidate the process physics of the PWJ, which uses a high-frequency high-pressure water jet to modify the target surfaces. The PWJ differs from a continuous plain water jet in that it contains an ultrasonic generator that produces ultra high-frequency mechanical core oscillations within the jet. The geometry, operating frequency, operating pressure, and nozzle-substrate distance of the nozzle affect the water slug formation process and the shape and size of the droplets. The flow is generated inside a nozzle with a solid inner probe moving at a high frequency. The modulated water flow results

in discrete packets of water, which degenerate into tiny droplets. The impact of small droplets results in material delamination or removal, depending on the process. The process does not use any chemicals, and because water can be recycled and reused, the process is environmentally friendly. Cold spray, in particular, is a possible application that could greatly benefit from PWJ surface preparation. Cold spray is a method of surface deposition that uses a supersonic gas jet to launch the surface coating on the substrate. The PWJ can be used to roughen the surface, which increases coating adhesion[26].

Surface damage, consistent with cavitation damage, has been observed on the forward tip of the nozzle's oscillating probe. Cavitation bubbles could be generated during the repeated high-speed retreat of the nozzle probe. It has been theorised that such cavitation bubbles may survive through the nozzle exit and could enhance surface erosion through bubble collapse and microscopic liquid jet generation, causing impact surface erosivity. The dynamics of the formation of the water jet leaving the nozzle, as well as its breakup into a spray of particles, is paramount to the erosive quality of the jet.

1.1 Pulsed Waterjet

The pulsed waterjet was first developed by Vijay et al. [35], who outlined improving high-speed water jets by adding ultrasonic modulation to create a pulsed jet. Works on improving this method were done by Foldyna [10], who studied the pulsed waterjet. The PWJ is extremely powerful and can cut metal at low pressure. For example, if one were to cut cast iron with a thickness of 6 mm with a standard jet, it would need pressures over 200 MPa, while the PWJ typically require to operate at a lower pressure of 69 MPa [36].

Vijay and Foldyna outlined the four regions of the water jet flow:

1. A continuous segment zone.

2. A transition zone where the modulation starts to form water packets.

Figure 1.1: The jet of the PWJ with modulation taken from VLN [31].

3. A zone of pulses, which are also called slugs.

4. Disintegration of the pulses into water droplets.

Vijay and Lai noted that the jet with the oscillating probe produced mushroom-like pulses [36], which can be seen in Figure 1.1. This is due to the surface tension, inertial forces, and aerodynamic drag [36]. Before Vijay et al. [35], Nebeker and Rodriguez studied the forced modulation of a continuous jet [20, 21]. Nebeker and Rodriguez explained that the effectiveness is also due to the water hammer effect and the size of the impact being larger than a normal jet[21]. The water hammer effect is the pressure surge due to the impact of water against a surface.

1.2 Objective of this study

The main objectives of this study are to verify and validate a suitable model for the PWJ. The partial differential equations (PDEs) describing the model are numerically solved using the discontinuous-Galerkin-Hancock method. The physics within the PWJ requires a model that can accurately simulate the high-speed and high-pressures associated with the PWJ. The model should also be able to represent multiphase flow, which should include water, vapour, and air. Suspected damage from cavitation bubbles has been observed on the ultrasonic probe. Cavi-

tation bubbles are caused by a drop in pressure, inducing a phase transition from water to vapour. To thermodynamically close the model, an equation of state for both liquid and gas flows must be chosen. As shown, an appropriate model is essential to find due to the complex physics within the PWJ. The chosen model is described by Saurel [27]. The Saurel model uses the multiphase Euler PDEs, and the model is thermodynamically closed by the Noble-Abel stiffened-gas (NASG) equation of state (EOS). The NASG EOS accurately models both liquid and gas flows while maintaining the property of compressibility within each phase. To describe the phase change, the model has a stiff source term driven by the difference in Gibbs free energies. The discontinuous Galerkin-Hancock method is employed to solve the PDEs. The discontinuous Galerkin-Hancock method, which is third-order accurate, can also solve the stiff source term outlined in Saurel's model [27]. These models are evaluated and validated. After assessing the model, simulations of the PWJ ultimately reveal the complex dynamics within its nozzle.

1.3 Scope of this study

The thesis covers the validation of multiphase models for the simulation of the pulsed waterjet. In Chapter 2 of this thesis, several multiphase models are investigated from the literature, and their applicability is assessed. The chosen multiphase model is described by Saurel [27]. Saurel's model uses the mixture Euler equation and has a stiff source term used to drive the phase change. These PDEs require an equation of state to thermodynamically close them. Moreover, various equations of state are assessed, and the Noble-Abel stiffened gas equation of state is ultimately chosen to close the PDEs. Following this, in Chapter 3, the discontinuous-Galerkin-Hancock method is discussed. It is a third-order accurate numerical scheme. Each time step in the discontinuous-Galerkin-Hancock method requires the solution of two coupled, highly non-linear equations. Newton's method is employed to solve these equations numerically. Finally, in Chap-

ter 4, the numerical results for the validation of the PDEs and equation of state are shown along with the validation of the multiphase model. Initial validation of PDEs and verification of the current implementation is shown by solving classical Riemann problems. An investigation of the flow through a venturi nozzle is conducted and compared to experiments. This venturi nozzle exhibits quasi-periodic cavitation shedding and validates the phase transition model through comparison with the experimental results. Finally, a time-accurate computation of the flow through the PWJ is investigated. An oscillating boundary condition is used to model the prescribed oscillatory motion of the nozzle probe. A detailed mesh refinement study is carried out to ensure the reliability of numerical solutions. The goal of this study is to determine how the oscillating probe affects the properties of the jet.

Another question this thesis seeks to answer is: to what degree does cavitation play an important role within the nozzle, if any? Numerical simulations enhance the fundamental understanding of the PWJ process and allow for future study of process parameters of the PWJ without expensive experimental tests.

Chapter 2

A Compressible Liquid-Gas Model with Phase Change

Multiphase flow is the flow of two or more distinct fluids within a single system. These fluids can be any combination of liquids, gases, or solids. Multiphase flow occurs in various industrial and natural processes ranging from nuclear reactors to volcanic eruptions. The physical properties of the multiphase flow are more complex than those of the single-phase flow because of the interaction of the different phases and their physical properties, such as differences in density and surface tension. The flow from the PWJ shows signs of cavitation; therefore, a multiphase model with phase change is needed. Cavitation is the phenomenon of a phase change from a liquid to a vapour through a pressure drop driven by fast acoustic pressure waves. The liquid pressure drops lower than the saturation pressure, and the liquid then transitions to vapour. The transition allows the formation and subsequent collapse of vapour bubbles. The collapse of these bubbles causes intense pressure waves, which often damage turbo-machinery. Damage that may be the result of cavitation bubbles has been found within the PWJ nozzle on the ultrasonic oscillating probe.

The transition from a liquid to vapour or vapour to liquid occurs under the vapour dome. The vapour dome is a graphical representation of the liquid-vapour

mixture of water in a phase diagram such as the pressure-enthalpy graph. The vapour dome is where the equality of Gibbs free energies is achieved between liquid and vapour phases. Most of the multiphase models explored for this work focus on cavitation. Cavitation is often assumed to be isothermal. In the literature, most cavitation models rely on two-phase mixtures that transition at a uniform temperature [2]. In these models, energy conservation and the second law of thermodynamics are omitted. The equation of state of these models imitates the physicality of two-phase flows. In these models, the mixture sound speeds increase non-monotonically as a function of the vapour fraction. Other isothermal models, such as the homogeneous equilibrium model [7] and the homogeneous relaxation model [3], use three and four equation models, respectively. Cahn-Hilliard [5] model boiling flows using capillary fluids where energy conservation is respected, but contrary to cavitation models, the square sound speed may result in negative values. The van der Waals equation of state, a cubic equation of state, is sometimes used. However, the van der Waals sound speed is undefined in certain thermodynamic regions. Many other issues arise through these models, such as enlarging interfaces to allow for more accurate computations. The Saurel model [27] is a more unified approach. The model outlined by Saurel is a hyperbolic set of partial differential equations with a stiff local source term driven by differences in the Gibbs free energy. The equation of state used is the Noble-Abel stiffened-gas equation of state, which can accurately model liquids, vapours, and mixtures.

2.1 Multiphase Flows

The flows in the pulsed waterjet are characterized by extremely high pressures and speeds. The flow inside the nozzle is also driven by a high-frequency piezoelectric ultrasonic oscillating probe that causes acoustic pressure waves. Incompressible treatments are unable to represent these effects. The need for a model that incorporates acoustic pressure waves is apparent. Furthermore, the possible role

of cavitation in the PWJ is an important aspect of this work, and a model that can correctly describe this phenomenon is also needed. After researching available thermodynamic and multiphase flow models, the model chosen takes the form of the traditional Euler equations for compressible flow prediction and modifies the equation of state (which relates the density, pressure, and energy) to accurately model liquid or gaseous water. The multiphase flow extension adds the volume fraction of each phase at every location. The governing partial differential equations (PDEs) can be written in two dimensions as

$$\frac{\partial}{\partial t}\begin{bmatrix}\rho\\ \rho u_x\\ \rho u_y\\ \rho E\\ \rho Y_1\\ \vdots\\ \rho Y_n\end{bmatrix}+\frac{\partial}{\partial x}\begin{bmatrix}\rho u_x\\ \rho u_x^2+p\\ \rho u_x u_y\\ (\rho E+p)u_x\\ \rho Y_1 u_x\\ \vdots\\ \rho Y_n u_x\end{bmatrix}+\frac{\partial}{\partial y}\begin{bmatrix}\rho u_y\\ \rho u_x u_y\\ \rho u_y^2+p\\ (\rho E+p)u_y\\ \rho Y_1 u_y\\ \vdots\\ \rho Y_n u_y\end{bmatrix}=S\,. \tag{2.1}$$

In Eq. (2.1), the first row is mass conservation, the second and third rows are momentum conservation in the x and y directions, respectively. The fourth row is energy conservation, and the subsequent n rows are the conservation of each phase or species within the fluid. Here, ρ is the mixture fluid density, u_x is the velocity in x-direction, u_y is the velocity in the y-direction, E is the total specific energy, p is the pressure, and $Y_1, Y_2, ..., Y_n$ are the mass fractions of the various phases. The above system can be generalized for any number of phases, n. This generalization consists of $n+4$ equations. Therefore, only $m+3$ of these equations are independent. However, the sum of all volume fractions must be one. This is due to the fact that any mass fraction, Y_k, can be expressed as a function of the

other mass fractions as

$$Y_k = 1 - Y_1 - ... - Y_{k-1} + Y_{k+1} - ... - Y_n \,. \tag{2.2}$$

The independent variables are: ρ, u_x, u_y, mass fractions Y_i, p, E and T. There are $n+4$ unknowns and only $m+3$ independent equations. Therefore, an equation of state is needed to close the system.

The specific total energy of the mixture is further defined as

$$E = e + u_x^2/2 + u_y^2/2 \tag{2.3}$$

with e as the mixture specific internal energy, which is defined as

$$e = Y_1 e_1 + Y_2 e_2 + ... + Y_n e_n \,. \tag{2.4}$$

The total specific internal energy is the sum of the contributions of each phase. The mixture density, ρ, can also be written as a function of the volume fractions, α, as

$$\rho = \alpha_1 \rho_1 + \alpha_2 \rho_2 + ... + \alpha_n \rho_n \,. \tag{2.5}$$

Another equation exists for the specific volume, v, in the form:

$$v = Y_1 v_1 + Y_2 v_2 + ... + Y_n v_n \,. \tag{2.6}$$

The specific volume is the inverse of the density, $v = \rho^{-1}$.

The system of equations assumes that each phase has the same temperature $T_1 = T_2 = .. = T_n$ and pressure $p_1 = p_2 = ... = p_n$. The phase change is described by a local source term that balances the Gibbs free energy of the two phases. For

equations describing a liquid that can vaporize, the source term is

$$S = \rho\nu(g_{vap} - g_{liq})\,. \tag{2.7}$$

The stiff relaxation parameter, ν, controls the rate of phase change. The other terms in Eq. (2.7) is the mixture density, ρ, times the difference in each phase's Gibbs free energy of the liquid and vapour phase, g_{liq} and g_{vap}. The phase change is described by a local source term that is driven by differences in the Gibbs free energy of the two phases. This model has been shown in the literature to accurately resolve sharp interfaces between phases and has been successfully used to predict flows in similar regimes to those encountered [27] .

It should be noted that, as this model is based on the Euler equations, it neglects the effects of viscosity, turbulence and heat transfer. Flow through the PWJ is expected to be highly turbulent, leading to very thin boundary layers. However, the short length of the nozzle gives confidence that viscous losses should not be a dominant effect. Future models could be improved by the inclusion of these effects. However, the current model should be accurate enough to make meaningful predictions.

2.1.1 Pulsed Waterjet Model

The PWJ is modelled with three phases: water, vapour, and air. The PDEs take the form:

$$\frac{\partial}{\partial t}\begin{bmatrix}\rho\\ \rho u_x\\ \rho u_y\\ \rho E\\ \rho Y_{air}\\ \rho Y_{liq}\end{bmatrix} + \frac{\partial}{\partial x}\begin{bmatrix}\rho u_x\\ \rho u_x^2 + p\\ \rho u_x u_y\\ (\rho E + p)u_x\\ \rho Y_{air}u_x\\ \rho Y_{liq}u_x F\end{bmatrix} + \frac{\partial}{\partial y}\begin{bmatrix}\rho u_y\\ \rho u_x u_y\\ \rho u_y^2 + p\\ (\rho E + p)u_y\\ \rho Y_{air}u_y\\ \rho Y_{liq}u_y\end{bmatrix} = \begin{bmatrix}0\\ 0\\ 0\\ 0\\ 0\\ \rho\nu(g_{vap} - g_{liq})\end{bmatrix}. \tag{2.8}$$

The vapour fraction, Y_{vap}, is arbitrarily chosen as the dependent variable, which is given by

$$Y_{vap} = 1 - Y_{liq} - Y_{air}$$

The v and e equation are as follows:

$$v = Y_{air}v_{air}(P,T) + Y_{liq}v_{liq}(P,T) + Y_{vap}v_{vap}(P,T)$$
$$e = Y_{air}e_{air}(P,T) + Y_{liq}e_{liq}(P,T) + Y_{vap}e_{vap}(P,T)$$

The fourth equation, which describes the flow of air, can be omitted for situations when only liquid and gaseous water are present.

Application to Axisymmetric Flows

The PWJ flow does not vary with angular coordinates. This study employs an axisymmetric treatment to simulate the behaviour of pulsed waterjets accurately. This approach is important as it simplifies the model from a three-dimensional problem to a two-dimensional problem while still retaining the physical characteristics of the jet. The axisymmetric flow condition assumes the pulsed waterjet is symmetric along its x-axis. This simplification allows for the better allocation of computational power to other more interesting areas within the simulation.
Axisymmetry changes the form of the PDEs to

$$\frac{\partial}{\partial t}\begin{bmatrix}\rho\\ \rho u_x\\ \rho u_r\\ \rho E\\ \rho Y_{air}\\ \rho Y_{liq}\end{bmatrix}+\frac{\partial}{\partial x}\begin{bmatrix}\rho u_x\\ \rho u_x^2+p\\ \rho u_x u_r\\ (\rho E+p)u_x\\ \rho Y_{air}u_x\\ \rho Y_{liq}u_x\end{bmatrix}+\frac{\partial}{\partial r}\begin{bmatrix}\rho u_r\\ \rho u_x u_r\\ \rho u_r^2+p\\ (\rho E+p)u_r\\ \rho Y_{air}u_r\\ \rho Y_{liq}u_r\end{bmatrix}=\begin{bmatrix}-\frac{1}{r}\rho u_r\\ -\frac{1}{r}\rho u_r u_x\\ -\frac{1}{r}\rho u_r^2+\\ -\frac{1}{r}(\rho E+p)u_r\\ -\frac{1}{r}\rho u_r Y_{air}\\ -\frac{1}{r}\rho u_r Y_{liq}+\rho\nu(g_{vap}-g_{liq})\end{bmatrix}. \tag{2.9}$$

The new cardinal directions are the x-direction and the r-direction. The source of the system is now filled with geometric source terms resulting from taking the fluxes' divergence in axisymmetric coordinates. These terms do not fundamentally change the nature of the flow and do not change the algorithm for Newton's method solver outlined within this study in Chapter 3.

2.2 Equation of State

This section evaluates various equations of state to ultimately find one best suited for the physics within the PWJ. The system of equations described in Eq. (2.1) is not closed. An equation of state that links pressure to density and energy is needed. Multiphase flows also provide a novel problem of needing an equation of state that can adequately define all the phases in the system. The ideal gas law is a potential candidate and can be used to close certain fluid systems. The ideal gas equation of state is

$$P=\frac{(\gamma-1)e}{v} \tag{2.10}$$

where γ is the ratio of specific heats. The ideal gas equation of state is limited by the assumption that the mean free path of the gas is disproportionally large compared to the scale of the molecular interactions, that intermolecular forces of the system are weak, and the volume of each gas molecule is negligible. The

ideal gas law cannot accurately model liquids. Other equations of state have compensated for the deficiencies of the ideal gas equation of state, notably the Noble-Abel equation of state and the stiffened-gas equation of state. The Noble-Abel equation of state is defined as

$$P = \frac{(\gamma - 1)e}{v - b}\,, \tag{2.11}$$

where b is a gas constant which defines the volume occupied by the gas molecules themselves. The constant b is a correction to the assumption that the volume of the molecule is negligible, which is an assumption that the ideal gas equation of state holds. The Noble-Abel equation of state is useful in situations with negligible intermolecular forces. The Noble-Abel equation of state is often used in the computation fluid modelling of propellant gas in gun chambers or within a context using combustion [28]. The stiffened-gas equation of state can be expressed as

$$P = \frac{(\gamma - 1)e}{v} - \gamma P_\infty\,, \tag{2.12}$$

where γP_∞ represents the inter-molecular forces. Ratio of specific heats is denoted by γ and P_∞ is the constant of the stiffened-gas. The stiffened-gas equation of state can be used for both the liquid and gaseous phases. The stiffened-gas constant, P_∞, is zero for gaseous states, but for a liquid, it mirrors a compressible liquid by assuming that a large pressure is already acting within the fluid.

The Noble-Abel stiffened-gas equation of state extends the Noble-Abel equation of state by adding the stiffened-gas constants. This combines the intermolecular forces, γp_∞, of the stiffened-gas equation of state with the Nobel-Abel equation of state volume correction, b. This allows for an equation in the form,

$$P = \frac{(\gamma - 1)(e - q)}{v - b} - \gamma P_\infty. \tag{2.13}$$

The parameters γ, q, b, and p_∞ are all constant coefficients of the fluid that

have been tuned to match experimental data for a wide range of states. The term $(\gamma-1)(e-q)$ represents thermal agitation, while $(v-b)$ represents repulsive short-distance effects linked to intermolecular motion. The term γp_∞ models attractive effects leading to matter cohesion in condensed states. The Noble-Abel stiffened-gas equation of state has a similar form to the van der Waals equation of state, which is of the form,

$$P = \frac{RT}{v-b} - \frac{a}{v^2}. \tag{2.14}$$

The cubic van der Waals equation differs in the $\frac{a}{v^2}$ inter-molecular forces term. The van der Waals equation of state correctly predicts the incompressible liquid phase but has difficulty predicting mixture phases within the vapour dome. The van der Waals equation of state considers the intermolecular forces within the phases and extends the ideal gas law. The van der Waals equation of state produces isotherms that oscillate within the mixture zone; this can be seen in Figure 2.1. Isotherms below the critical state are oscillatory and physically not true, while isotherms above the critical state are stable. This oscillation produces speeds of sound that are negative and not real [27]. The Nobel Abel stiffened-gas equation of state is a convex equation with positive and real sound speeds, unlike the Van Der Waal Equation of state [18].

Ultimately, the Noble-Abel stiffened-gas equation of state is chosen. The Noble-Abel stiffened-gas EOS can accurately model compressible multiphase and multicomponent flows in an inert [12] and reactive context [4]. The Noble-Abel stiffened-gas equation of state is a reliable equation of state that can accurately predict the compressibility of fluids in the proper context.¡

2.3 Noble-Abel Stiffened-Gas Equation of State

As stated previously, PDEs describing the chosen multiphase fluid model, Eq. (2.1), are not closed. An equation of state linking the pressure to the density and energy

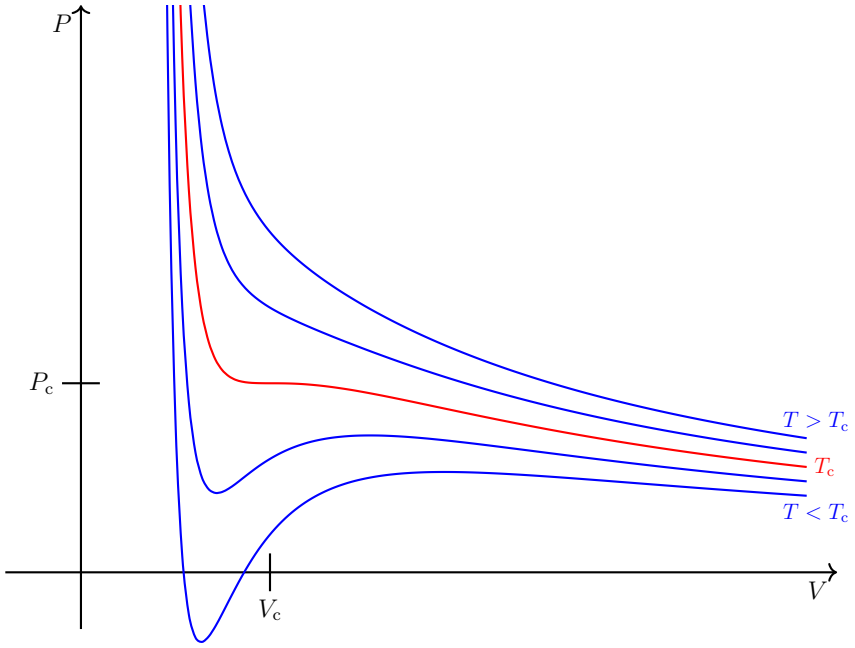

Figure 2.1: A Pressure vs volume graph of van der Waal isotherms [22].

is needed. The Noble-Abel stiffened-gas equation of state is designed to accurately model liquids at very high speeds and pressures[18]. The Noble-Abel stiffened-gas equation of state adds the repulsive effects of the stiffened-gas equation of state to the Noble-Abel equation of state. The Noble-Abel stiffened-gas equation of state is a modification of the ideal gas law, and it is particularly well-suited for flows in which high-speed pressure waves are relevant. The speed of sound for the NASG EOS can be expressed as

$$c = \sqrt{\left(\frac{\partial P}{\partial \rho}\right)_s} = \sqrt{\gamma \frac{p - p_\infty}{v - b} v^2}\,. \tag{2.15}$$

This expression agrees with the traditional speed of sound for an ideal gas in the gaseous regions of the flow. The expression for the Gibbs free energy takes the form

$$g = (\gamma C_v - q')T - C_v T \ln \frac{T^\gamma}{(p + p_\infty)^{\gamma - 1}} - bp + q\,. \tag{2.16}$$

where C_v is the constant volume specific heat.The expression for the temperature

can be written as

$$T = \frac{(p + p_\infty)}{C_v(\gamma - 1)}(v - b)\,. \tag{2.17}$$

The expression for specific energy is written as

$$e = \frac{(p + \gamma p_\infty)C_v T}{(p + p_\infty)} + q\,. \tag{2.18}$$

The expression for a specific volume is written as

$$v = \frac{(\gamma - 1)C_v T}{p + p_\infty} + b\,. \tag{2.19}$$

2.3.1 Mixture Noble-Abel Stiffened-Gas

A mixture equation of state is needed to close the mixture Euler equations. The current mixture equation of state assumes that each phase has the same temperature $T_1 = T_2 = T$ and pressure $p_1 = p_2 = p$. The mixture temperature equation can be retrieved by inserting Eq. (2.17) into the equation

$$v = Y_1 v_1 + Y_2 v_2\,. \tag{2.20}$$

Solving for T gives a mixture temperature,

$$T = (v - \bar{b})\left(\sum_i \frac{Y_i C_{vi}(\gamma_i - 1)}{p + \gamma_i p_{\infty_i}}\right)^{-1}\,. \tag{2.21}$$

The same can be done for the mixture energy equation,

$$e = Y_1 e_1 + Y_2 e_2\,, \tag{2.22}$$

which gives another equation for the temperature,

$$T = (e - \bar{q}) \left(\sum_i \frac{Y_i C_{vi}(p + \gamma_i p_{\infty_i})}{p + \gamma_i p_{\infty_i}} \right)^{-1} . \tag{2.23}$$

Here, $\bar{q}$ and $\bar{b}$ are defined as

$$\bar{q} = Y_1 q_1 + Y_2 q_2 \,, \tag{2.24}$$

$$\bar{v} = Y_1 v_1 + Y_2 v_2 \,. \tag{2.25}$$

Equating Eq. (2.21) and Eq. (2.23) to eliminate the temperature and isolate for the pressure, p, produces a polynomial. The degree of the polynomial is equal to the number of phases. The polynomial is cubic in a scenario with three phases: liquid water, vapour, and air. In the current scenario with liquid water and vapour, the polynomial is quadratic in the form of:

$$a_2 p^2 + a_1 p + a_0 = 0 \,. \tag{2.26}$$

The constants for a mixture with two phases take the form,

$$\begin{aligned} a_2 &= Y_1 C_{v_1} + Y_2 C_{v_2} \,, \\ a_1 &= Y_1 C_{v_1}(p_{\infty_2} + \gamma_1 p_{\infty_1} - (\gamma_1 - 1)Q) \\ &\quad + Y_2 C_{v_2}(p_{\infty_1} + \gamma_2 p_{\infty_2} - (\gamma_2 - 1)Q) \,, \\ a_0 &= -Q((\gamma_1 - 1)Y_1 C_{v1} p_{\infty_2} + (\gamma_2 - 1)Y_2 C_{v2} P_{\infty_1} \\ &\quad + p_{\infty_1} p_{\infty_2}(\gamma_1 Y_1 C_{v_1} + \gamma_2 Y_2 C_{v_2}) \,, \end{aligned} \tag{2.27}$$

where

$$Q = \frac{e - \bar{q}}{v - \bar{b}} \,. \tag{2.28}$$

The equation for pressure is the quadratic equation for two phases in the form

$$p = \frac{-a_1 + \sqrt{a_1^2 - 4a_0a_2}}{2a_2}\,. \tag{2.29}$$

After the pressure is determined, the temperature is calculated from either Eq. (2.21) or Eq. (2.23). The mixture sound speed can be written as the mechanical equilibrium sound speed described as the Wood's mixture sound speed [37], which obeys the formula

$$\frac{1}{\rho c_w^2} = \sum_k \frac{a_k}{\rho_k c_k^2}\,, \tag{2.30}$$

with sound speed, c_k , density, ρ_k, and volume fractions, α_k, for each phase. The wood sound speed is c_w.

In the previous chapter, the PDEs and the equation of state were outlined. The next chapter will focus on methods to solve these models.

Chapter 3

Numerical Methods

Multiphase models are widely used to model cavitating and boiling flows. Most of these models are solved numerically on a spatial discretization scheme, such as the finite-volume method, to find the numerical solution. In this work, the discontinuous-Galerkin Hancock method is preferred for its high-order spatial and temporal accuracy, as well as its high parallel efficiency. It is specifically designed to efficiently handle stiff source terms, such as the one described in Saurel's model [27], which is used in this thesis.

Reed and Hill introduced the original discontinuous-Galerkin (DG) method to solve the steady linear neutron transport equation [25]. The degree k DG methods have a convergence rate of $(\Delta x)^k$ for general triangulation and $(\Delta x)^{k+1}$ for Cartesian grids, which was found by LeSaint and Raviart [19]. The rate of convergence for general triangulation is $(\Delta x)^{k+\frac{1}{2}}$, which was proven by Johnson and Pitkaränta [16] and later confirmed by Peterson [23]. One of the most popular models in the family of DG methods was developed by Cockburn and Shu, called the Runge-Kutta discontinuous-Galerkin (RKDG) method [6]. The model uses a piecewise linear DG method for the spatial discretization and an explicit total variation diminishing (TVD) second-order Runge-Kutta scheme for temporal discretization. To achieve higher-order accuracy, DG schemes can use higher-order polynomials and Runge-Kutta methods.

The RKDG schemes use the DG discretization in space only to produce a semi-discrete model that takes the form of a large set of coupled ordinary differential equations (ODEs). This technique is also known as the method of lines (MOL), which is outlined by Schiesser [29]. The technique described by Schiesser has limitations, such as reduced stability and limited time step size; the DG method for spatial discretization becomes more restrictive as it increases the order of accuracy.

Fully discrete methods for space-time discretization are used to avoid the setbacks associated with the MOL approach. For example, the Lax-Wendroff method is second-order in space and time and employs full discretization in space and time [17]. The Lax-Wendroff method relates temporal derivatives in terms of spatial derivatives. Another method that is fully discrete for space-time discretization is the arbitrarily high order (ADER) method, which was developed by Toro *et. al* [32]. Dumbser and Munz combined the DG framework with ADER [8] to create the ADER-DG method, which is a one-step method and reduces the use of a TVD limiter, making it more efficient than the RKDG method. A Fourier analysis proved that the fully discrete ADER-DG method has an equivalent stability restriction as RKDG methods [9].

The set of PDEs outlined in Eq. (2.1) are hyperbolic equations with a stiff relaxation source term. The discontinuous-Galerkin Hancock (DGH) model developed by Suzuki and Van Leer solves this set of PDEs [30]. The DGH scheme uses a coupled space-time approach. The DGH method is derived from Huynh's upwind moment scheme [15] for hyperbolic conservation equations. The DGH scheme is third-order accurate in space and time and is well-suited for parallel computation. This is partilaly due to the fact that it is a single step method, with an intermediate substep to $t^{n+\frac{1}{3}}$, requiring inter-process messages to be passed only once per time step.

3.1 Discontinuous-Galerkin Hancock Method for Two-Dimensional Equations

3.1.1 Weak Formulation

The DGH method is a coupled space-time method for the solution of hyperbolic balance equations with stiff local source terms, similar to the model described in this paper. The DGH method solves the weak solutions to PDEs of the form

$$\frac{\partial U}{\partial t} + \frac{\partial F_i}{\partial x_i} = S\,. \tag{3.1}$$

The weak solutions are chosen so that the product of the PDEs with a a finite set of test functions integrated over the space-time domain $\Omega(t) \times T$ are satisfied. The time domain is denoted as T and $\Omega(t)$ is the space domain. The scalar test function spans the space of the solution $U(x_j, t)$, which is written as $v(x_j, t) \in \Omega(t) \times T$. Integrating the product of the PDE with an arbitrary test function over the space-time domain yields the weak solution, which is taken as

$$\iint_{\Omega(t)\times T} v(x_j,t)\frac{\partial U}{\partial t}\mathrm{d}x_j\mathrm{d}t = -\iint_{\Omega(t)\times T} v(x_j,t)\frac{\partial F_i}{\partial x}\mathrm{d}x_j\mathrm{d}t + \iint_{\Omega(t)\times T} v(x_j,t)S\mathrm{d}x_j\mathrm{d}t \tag{3.2}$$

For each time step, the time interval is between $[t^n, t^{n+1}] \in T$. The weak formulation requires taking a finite number of test functions $v(x_j, t) \in \Omega(t) \times T$ that satisfy Eq. (3.2).

The spatial domain of integration, $\Omega(t)$ can be further simplified as $\Omega_k(t)$ because the test functions are chosen to be non-zero in only one cell. Eq. (3.2) is solved by integration by parts, which removes the derivatives of the solution and its flux from the space-time integrals,

$$\int_T v(x_j,t)\frac{\partial U}{\partial t}\mathrm{d}t = \left[U^{n+1}v(x_j,t) - U^n v(x_j,t)\right] - \int_T U\frac{\partial}{\partial t}v(x_j,t)\mathrm{d}t\,, \tag{3.3}$$

$$\int_{\Omega_k(t)} v(x_j,t)\frac{\partial F_i}{\partial x}\mathrm{d}x_j = \int_{\Gamma_k(t)} v(x_j,t)F_i\cdot\hat{n}_i d\Gamma - \int_{\Omega_k(t)} F_i\frac{\partial}{\partial x}v(x_j,t)\mathrm{d}x_j\,. \tag{3.4}$$

The boundary of the two-dimensional cell is Γ_k, and $\hat{n}_i$ is the unit vector normal to the surface of the cell. The test functions are assumed to be constant in time and are functions of only space, $v(x_j,t) = v(x_j)$. By subbing Eq. (3.3) and Eq. (3.4) into Eq. (3.2) and using Fubini's theorem, which switches the order of integration in space and time, the weak formulation becomes

$$\begin{aligned}\int_{\Omega_k} v(x_j)\left[U^{n+1}-U^n\right]\mathrm{d}x_j = &-\iint_{\Gamma_k\times T} x(x_j)F_i\cdot n_i d\Gamma\mathrm{d}t + \iint_{\Omega_k\times T} F_i\frac{\partial}{\partial t}v(x_j)\mathrm{d}x_j\mathrm{d}t\\ &+\iint_{\Omega_k\times T} v(x_j)S\mathrm{d}x_j\mathrm{d}t\,.\end{aligned} \tag{3.5}$$

Polynomial Representation of solution

Appropriate test functions are needed for the discretization of the weak formulation, Eq. (3.5). The solution $U_h(x_h,t)|_{\Omega_k}$ within element Ω_k is assumed to be a polynomial function. The Legendre polynomials P, which are piecewise linear functions, for the degree of $k=1$ and two-dimensional problem, $x_j = [x,y]$, are

$$U_h(x_j,t)|_{\Omega_k}, v(x_j)|_{\Omega_k} \in P^1(\Omega_k) \tag{3.6}$$

where

$$\begin{aligned}P^1(\Omega_k) &= \mathbf{span}\{\theta_0(x_j),\theta_1(x_j),\theta_2(x_j)\}\\ &= \mathbf{span}\{1, x-x_{ck}, y-y_{ck}\}\,.\end{aligned} \tag{3.7}$$

The constants (x_{ck}, y_{ck}) are the centroid of the element Ω_k and are defined as

$$x_{ck} = \frac{\iint_{\Omega_k} x \mathrm{d}x dy}{\iint_{\Omega_k} \mathrm{d}x dy}\,, \quad y_{ck} = \frac{\iint_{\Omega_k} y \mathrm{d}x dy}{\iint_{\Omega_k} \mathrm{d}x dy}\,. \tag{3.8}$$

The assumed solutions in cell k is, thus,

$$U_k = \overline{U}_k + (\overline{\Delta_x U})_k (x - x_{ck}) + (\overline{\Delta_y U})_k (y - y_{ck})\,. \tag{3.9}$$

Here, $\overline{U}_k$ is the cell averaged value and $[(\overline{\Delta x U})_k, (\overline{\Delta y U})_k]$ are the average values of the solution gradient of each cell in the x and y direction.

Update Formulas for the Degrees of Freedom

Substitution of the solutions assumed the form of Eq. (3.9) into Eq. (3.5) and then integrating with each test function produces the updated formula for the degrees of freedom.

$$\overline{U}_k^{n+1} = \overline{U}_k^n - \frac{1}{A_k} \iint_{\partial\Gamma_k \times T} F_i \cdot \hat{n}_i d\Gamma \mathrm{d}t + \frac{1}{A_k} \iint_{\partial\Omega_k \times T} S \mathrm{d}x_j \mathrm{d}t\,, \tag{3.10}$$

and

$$\begin{aligned}\begin{bmatrix}\overline{\Delta_x U_k}^{n+1}\\ \overline{\Delta_y U_k}^{n+1}\end{bmatrix} &= \begin{bmatrix}\overline{\Delta_x U_k}^{n}\\ \overline{\Delta_y U_k}^{n}\end{bmatrix}\\ &+ \overline{K_k}\left(- \iint_{\partial\Gamma_k\times T} \begin{bmatrix} x-x_{ck}\\ y-y_{ck}\end{bmatrix} F_i\cdot\hat{n}_i d\Gamma \mathrm{d}t\right.\\ &+ \iint_{\partial\Omega_k\times T} \begin{bmatrix} F_x\\ F_y\end{bmatrix} \mathrm{d}x_j\mathrm{d}t\\ &\left.+ \iint_{\partial\Omega_k\times T} \begin{bmatrix} x-x_{ck}\\ y-y_{ck}\end{bmatrix} S\mathrm{d}x_j\mathrm{d}t\right)\end{aligned} \tag{3.11}$$

Here, A_k is the area of the cell, which is defined as

$$A_k = \iint_{\Omega_k} \mathrm{d}x\mathrm{d}y\,. \tag{3.12}$$

Here $\partial\Gamma_k$ is the edges of the boundary Γ_k, and $\overline{K_K}$ is a matrix filled with the area moments of inertia of the cell, which can be written as

$$\overline{K}_k = \begin{bmatrix} I_{xx} & I_{xy}\\ I_{yx} & I_{yy}\end{bmatrix}\,, \tag{3.13}$$

where

$$I_{xx} = \iint_{\Omega_k} (x-x_{ck})^2\mathrm{d}x_j \tag{3.14}$$

$$I_{xy} = I_{yx} = \iint_{\Omega_k} (x-x_{ck})(y-y_{ck})\mathrm{d}x_j \tag{3.15}$$

$$I_{yy} = \iint_{\Omega_k} (y-y_{ck})^2\mathrm{d}x_j \tag{3.16}$$

are the area moments of inertia of the cell. Equations. (3.10) and (3.11) contain several integrands that must be approximated with quadrature rules.

Interface-Flux Approximation and Surface Integral

Numerical approximations are required for interface fluxes because solutions between cells are discontinuous in a DG scheme. The interface flux along $\partial\Gamma_k$ is obtained by using an approximate Riemann solver,

$$F_i \cdot \hat{n}_i \approx \tilde{F}_\zeta \,. \tag{3.17}$$

Where $\tilde{F}_\zeta$ is the vector of fluxes normal to the edge of Γ_k. A non-linear flux integral is approximated by a quadrature rule. The quadrature for the spatial integration along the edges must be exact for a polynomial of degree 2k+1 if the solution is represented in polynomial space P^k [6]. The spatial integration is approximated with a two-point Gaussian quadrature to achieve third-order accuracy. The quadrature rule is

$$\iint_{\partial\Gamma_k \times T} F_i \cdot \hat{n}_i d\Gamma \mathrm{d}t \approx \int_T \sum_\zeta w_\zeta \tilde{F}_\zeta \mathrm{d}t. \tag{3.18}$$

where w_ζ is the weight given to the quadrature point ζ. The time integration uses the midpoint rule, which is evaluated at $t^{n+\frac{1}{2}}$.

$$\iint_{\partial\Gamma_k \times T} F_i \cdot \hat{n}_i d\Gamma \mathrm{d}t \approx \Delta t \sum_\zeta w_\zeta \tilde{F}_\zeta^{n+\frac{1}{2}} \tag{3.19}$$

These fluxes are again employed in the slope update, in Eq. (3.11), for approximating the surface integral.

$$\iint_{\partial\Gamma_k \times T} \begin{bmatrix} x - x_{ck} \\ y - y_{ck} \end{bmatrix} F_i \cdot \hat{n}_i d\Gamma \mathrm{d}t = \Delta t \begin{bmatrix} \sum_\zeta w_\zeta (x - x_{ck}) \tilde{F}_\zeta^{n+\frac{1}{2}} \\ \sum_\zeta w_\zeta (y - y_{ck}) \tilde{F}_\zeta^{n+\frac{1}{2}} \end{bmatrix}. \tag{3.20}$$

Therefore, the surface flux integrals in Eq (3.10) are evaluated using a combination of two-point Gaussian quadrature on each cell edge in space and midpoint rule in time, which is illustrated in Figure 3.1. Each cell edge has two quadrature points

with a total of eight quadrature points for a quadrilateral. At each quadrature point, a Riemann solver is employed to compute the interfacial flux. The weights of each Gaussian quadrature point is $\frac{1}{2}$ the edge length. The solution is discontinuous on the edge of a cell; thus, a numerical Riemann solver is used.

Hancock's Predictor Step

The solution at the half-time steps $U_h(x_i, t^{n+\frac{1}{6}})$ and $U_h(x_i, t^{n+\frac{1}{2}})$ are required as inputs for the approximate Riemann solver to complete the approximation of the surface integral. Hancock's implicit predictor step is used to find the values of the solution at the half time-step.

In Figure 3.2, the Hancock predictor technique is illustrated using the one-dimensional Euler equations as examples, therefore three characteristic lines are drawn. Wave interactions can be ignored up to the half-time step $t^{n+\frac{1}{2}}$. Hancock observed that the flow quantities at cell centres evolve over the half-time step independent of their neighbour cells. The updated formula for the cell-average value in Eq. (3.10) can be adjusted to remove element-face interactions, which results in

$$\bar{U}_k^{n+\Psi} = \bar{U}_k^n - \frac{1}{A_k}\left(\iint_{\partial\Gamma_k \times T'} \hat{F}_i \cdot \hat{n}_i d\Gamma \mathrm{d}t + \iint_{\Omega_k \times T'} S \mathrm{d}x_j \mathrm{d}t\right) . \tag{3.21}$$

The time interval here is $T' \in [t^n, t^{n+\Psi}]$ with values of $\Psi = \frac{1}{6}$ or $\Psi = \frac{1}{2}$, and the flux tensor, $\hat{F}_i$, is computed by employing the Gaussian quadrature points in Eq. (3.10). The predictor step in Eq. (3.10) can be further approximated by evaluating the flux integral from time t^n to have the form:

$$\bar{U}_k^{n+\Psi} = \bar{U}_k^n + \frac{\Delta t}{A_k}\left[-\int_{\partial\Gamma_k} \hat{F}_i(U_h(x_j, t^n)) \cdot \hat{n}_i \mathrm{d}\Gamma + \int_{\Omega_k} S(U_h(x_j, t^{n+\Psi}))\mathrm{d}x_j\right] . \tag{3.22}$$

After the predicted cell average state at a fractional-time step $U_k^{n+\Psi}$ is computed,

the solution at any point along $\partial\Gamma_k$ can be procured with

$$U_h(x_j, t^{n+\Psi}) = \overline{U}_k^{n+\Psi} + \theta_k^n \begin{bmatrix} \overline{\Delta_x U}_k^n \\ \overline{\Delta_y U}_k^n \end{bmatrix} \cdot \begin{bmatrix} x - x_{ck} \\ y - y_{ck} \end{bmatrix} . \tag{3.23}$$

where θ_k^n is a vector of slope limiter values. The slope variables are calculated at time t^n. The slope limiter used is the Venkatakrishnan limiter [34], which is an extension of the one dimensional Van Albada limiter [1]. Minmod is also implemented as a slope limiter [33]. A slope limiter is used to ensure monotonicity and avoid oscillations near discontinuities in high-order total variance diminishing finite-element schemes, which includes the DGH scheme, that use slopes to find their assumed solution.

The spatial integration of the source term is evaluated at one Gaussian quadrature point at the centroid of the element $(x_c k, t^{n+\Psi})$ Ω_k. It takes the form:

$$\int S \mathrm{d}x_j \approx A_k S(U_k^{n+\Psi}(x_c k, t^{n+\Psi}))\,. \tag{3.24}$$

After inserting the above into Eq (3.22), the state at $U_h(x_i, t^{n+\Psi})$ can be found as

$$\begin{aligned} \bar{U}_k^{n+\Psi} = \bar{U}_k^n + \theta_k^n \begin{bmatrix} \overline{\Delta_x U}_k^n \\ \overline{\Delta_y U}_k^n \end{bmatrix} \cdot \begin{bmatrix} x - x_{ck} \\ y - y_{ck} \end{bmatrix} \\ -\frac{\Delta t}{A_k} \sum_{\partial\Gamma_k \in \partial\Gamma_k} \int_{\partial\Gamma_k} \hat{F}_i \cdot \hat{n}_i d\Gamma + \Delta t S(U_k^{n+\Psi}(x_c k, t^{n+\Psi})). \end{aligned} \tag{3.25}$$

The Hancock predictor step is computed at the start of each time step and the solutions at the half-time steps are stored.

Area Integral of Flux and Source Term

The stiff local source term in this model is solved implicitly. This method does not add excessive computation as it is local and does not couple between cells. Suzuki chose the Radau IIA method for the source-term time integration [30]

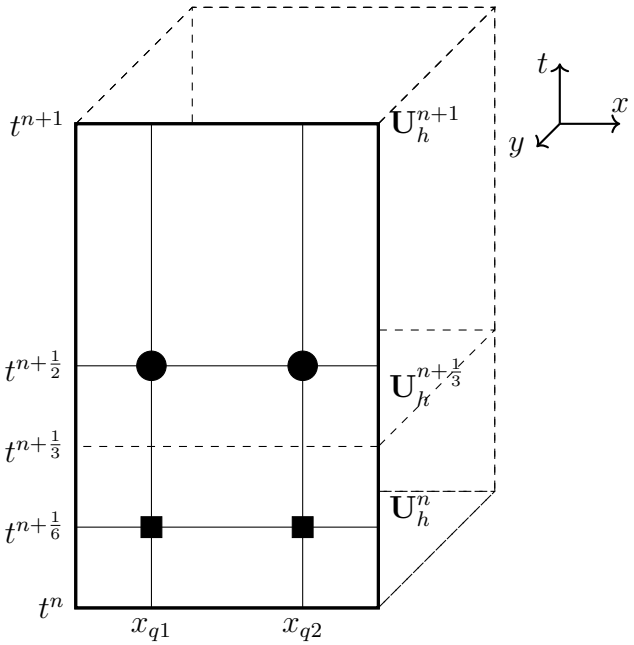

Figure 3.1: Diagram showing the area integral calculated using 2-point Gaussian quadrature rule in space and midpoint rule in time. The x_{q_1} and x_{q_2} are the quadrature points. The space-time elements in dashed lines are known or computed. The squares represent the quadrature points used in the integration along $[t^n, t^{n+\frac{1}{3}}]$ and the circles represent the quadrature points used in the integration along $[t^n, t^{n+1}]$.

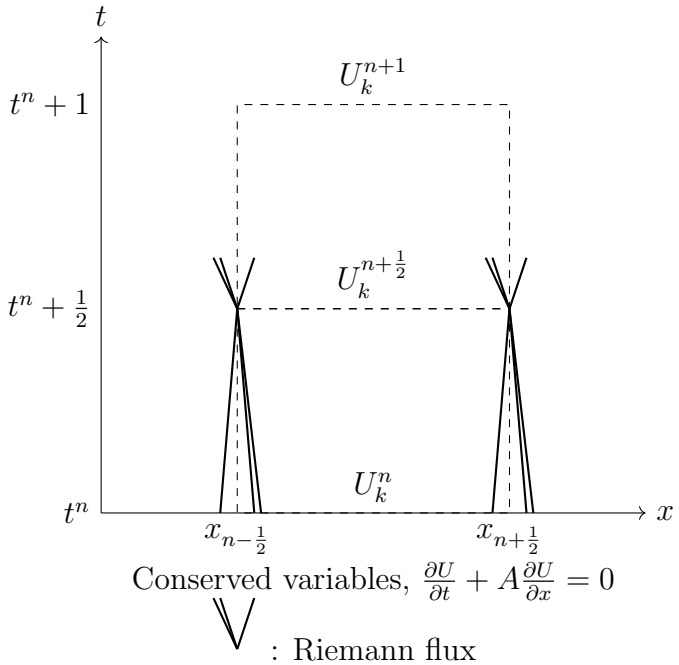

Figure 3.2: Visual representation for Hancock's technique of predicting values at the half-time step, $t^{n+\frac{1}{2}}$. The values obtained at the half-time step are used as the input for the Riemann problems at $(x_{k+\frac{1}{2}}, t^{n+\frac{1}{2}})$. These values are obtained using data stored locally within each cell

adding a required state at time $t^{n+\frac{1}{3}}$. This method is an L-stable, two-step, and a third-order accurate implicit time-marching scheme in the form

$$\begin{aligned} Y^{n+\frac{1}{3}} &= Y^{n+\frac{1}{6}} + \Delta t \left[\frac{5}{12}(S)^{n+\frac{1}{3}} - \frac{1}{12}(S)^{n+1} \right] , \\ Y^{n+1} &= Y^{n+\frac{1}{2}} + \Delta t \left[\frac{3}{4}(S)^{n+\frac{1}{3}} + \frac{1}{4}(S)^{n+1} \right] . \end{aligned} \tag{3.26}$$

The Radau-IIA method has an additional time step at $t^{n+\frac{1}{3}}$, which results in increasing the number of quadrature points by two points per edge.

Gaussian quadrature is used for area integration and the quadrature points can be seen in Figure 3.3. The scheme uses a four-point quadrature rule in a two-dimensional space. For a two-dimensional reference element in the domain of $[\alpha, \beta] \in [-1, 1]^2$ a four-point quadrature rule is used . The position for each of these quadrature points in reference space, $\zeta(\alpha, \beta)$, are

$$\zeta_0 = \left(-\frac{1}{\sqrt{3}}, -\frac{1}{\sqrt{3}} \right) , \ \zeta_1 = \left(\frac{1}{\sqrt{3}}, -\frac{1}{\sqrt{3}} \right) , \ \zeta_2 = \left(\frac{1}{\sqrt{3}}, \frac{1}{\sqrt{3}} \right) , \ \zeta_3 = \left(-\frac{1}{\sqrt{3}}, \frac{1}{\sqrt{3}} \right) . \tag{3.27}$$

The quadrilateral cells can be substituted for any convex four-sided polygon. This is accomplished by shifting to a local coordinate system from a physical domain in Ω to a computational domain $\hat{\Omega}$. The coordinate transform takes the form

$$x(\alpha, \beta) = \frac{1-\alpha}{2}\frac{1-\beta}{2}x_0 + \frac{1+\alpha}{2}\frac{1-\beta}{2}x_1 + \frac{1+\alpha}{2}\frac{1+\beta}{2}x_2 + \frac{1-\alpha}{2}\frac{1+\beta}{2}x_3 \, . \tag{3.28}$$

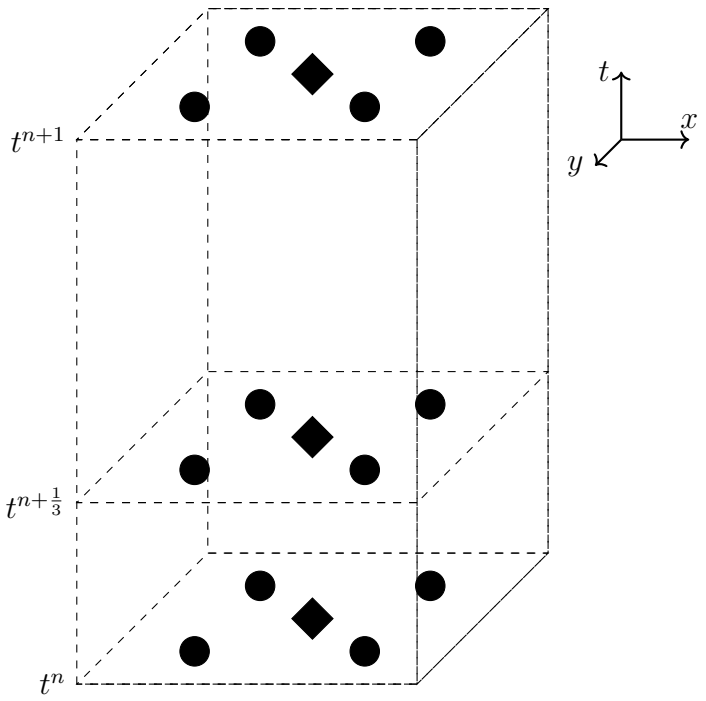

Figure 3.3: Diagram of the area integrals using Gaussian quadrature in space and Radau-IIA in time. Quadrature points that are used for the source-term integration are shown here as diamonds and points for flux integration are shown with circles.

Area Integral of the Flux

These four quadrature points are used to approximate the area integral,

$$\int_{\Omega_k} F_i(U(x_j,t))\mathrm{d}x_j = \int_{\hat{\Omega}_k} F_i(U(\zeta_j,t))|J(\zeta_j)|d\zeta_j \approx \sum_{i=0}^{3} w_i|J(\zeta_i)|F_i(U(\zeta_j,t))\,, \tag{3.29}$$

where w_i is the weight of the Gaussian quadrature point i, and $|J(\zeta_i)|$ is the determinant of the Jacobian

$$|J(\zeta_i)| = \frac{\partial x}{\partial \alpha}\frac{\partial y}{\partial \beta} - \frac{\partial x}{\partial \beta}\frac{\partial y}{\partial \alpha}\,. \tag{3.30}$$

Area integrals for the flux are used in the update formula for the slope quantities. The time integration is approximated by the Radau-IIA quadrature, as shown

$$\iint_{\Omega_k \times T} F_i \mathrm{d}x_j \mathrm{d}t \approx \Delta t \int_{\Omega_k} \left[\frac{3}{4}F_i^{n+\frac{1}{3}} + \frac{1}{4}F_i^{n+1}\right]. \tag{3.31}$$

The area integral can be approximated using the Gaussian quadrature in space as such,

$$\iint_{\Omega_k \times T} F_i \mathrm{d}x_j \mathrm{d}t \approx \Delta t \sum_i w_i |J(\zeta_i)| \left[\frac{3}{4} F_i^{n+\frac{1}{3}} + \frac{1}{4} F_i^{n+1} \right]. \tag{3.32}$$

For the time interval $T' \in [t^n, t^{n+\frac{1}{3}}]$ the area integral takes the form

$$\iint_{\Omega_k \times T'} F_i \mathrm{d}x_j \mathrm{d}t \approx \frac{\Delta t}{3} \sum_i w_i |J(\zeta_i)| \left[\frac{1}{2} F_i^{n} + \frac{1}{2} F_i^{n+\frac{1}{3}} \right]. \tag{3.33}$$

Area Integral of the Source Term

The update formula of the cell-average values includes the area integral of the source terms with the quadrature points that approximate the integral as seen in Figure 3.3. A simple linearization is performed to decouple the source term update from the other update formulas.

$$S(U_h(x_j, t)) \approx S(\overline{U}_k(t)) + \left(\frac{\partial S}{\partial U} \right)^n \left(\begin{bmatrix} \overline{\partial_x U}_k^n \\ \overline{\partial_y U}_k^n \end{bmatrix} \cdot \begin{bmatrix} x - x_{ck} \\ y - y_{ck} \end{bmatrix} \right) \tag{3.34}$$

$$\iint_{\Omega_k \times T} S \mathrm{d}x_j \mathrm{d}t \approx A_k \Delta t \left[\frac{3}{4} S(\overline{U}_k^{n+\frac{1}{3}}) + \frac{1}{4} S(\overline{U}_k^{n+1}) \right] \tag{3.35}$$

Area Integral of the Moment of the Source Term

The area integral of the moment of the source term is also present in the update formula of the slope quantities. A linearization is applied to make the update equation for the cell-averaged values independent of the other update formulas. The Radau-IIA method is used to approximate the solution in time. The spatial integration is done analytically.

$$\iint_{\Omega_k \times T} \begin{bmatrix} x - x_{ck} \\ y - y_{ck} \end{bmatrix} S \mathrm{d}x_j \mathrm{d}t \approx \Delta t \begin{bmatrix} \frac{3}{4}(\overline{\frac{\partial S}{\partial U}})_k^{n+\frac{1}{3}} (\overline{\partial_x U})_k^{n+\frac{1}{3}} + \frac{1}{4}(\overline{\frac{\partial S}{\partial U}})_k^{n+1} (\overline{\partial_x U})_k^{n+1} \\ \frac{3}{4}(\overline{\frac{\partial S}{\partial U}})_k^{n+\frac{1}{3}} (\overline{\partial_y U})_k^{n+\frac{1}{3}} + \frac{1}{4}(\overline{\frac{\partial S}{\partial U}})_k^{n+1} (\overline{\partial_y U})_k^{n+1} \end{bmatrix} \tag{3.36}$$

Discrete Update Formulas

By combining the above quadrature rules, the final update formula for the cell-averaged value is

$$\begin{bmatrix} \overline{U}_k^{n+\frac{1}{3}} \\ \overline{U}_k^{n+1} \end{bmatrix} = \begin{bmatrix} \overline{U}_k^{n} \\ \overline{U}_k^{n} \end{bmatrix} - \frac{\Delta t}{A_k} \begin{bmatrix} \frac{1}{3} \sum_\zeta w_\zeta \tilde{F}^{n+\frac{1}{6}} \\ \sum_\zeta w_\zeta \tilde{F}^{n+\frac{1}{2}} \end{bmatrix} + \Delta t \begin{bmatrix} \frac{5}{12} I & -\frac{1}{12} \\ \frac{3}{4} I & \frac{1}{4} \end{bmatrix} \begin{bmatrix} \overline{S}^{n+\frac{1}{3}} \\ \overline{S}^{n+1} \end{bmatrix}. \tag{3.37}$$

For complex non-linear source terms, such as the one described in this paper, Newton's method is employed to find a solution. The discrete form of the slope

updates is

$$\begin{aligned}
\begin{bmatrix} \overline{\Delta_x U_k}^{n+\frac{1}{3}} \\ \overline{\Delta_y U_k}^{n+\frac{1}{3}} \\ \overline{\Delta_x U_k}^{n+1} \\ \overline{\Delta_y U_k}^{n+1} \end{bmatrix} &= \begin{bmatrix} \overline{\Delta_x U_k}^{n} \\ \overline{\Delta_y U_k}^{n} \\ \overline{\Delta_x U_k}^{n} \\ \overline{\Delta_y U_k}^{n} \end{bmatrix} \\
&+\Delta t \Upsilon \begin{bmatrix} \frac{1}{3}\sum_\zeta w_\zeta \tilde{F}^{n+\frac{1}{6}} \\ \frac{1}{3}\sum_\zeta w_\zeta \tilde{F}^{n+\frac{1}{6}} \\ \sum_\zeta w_\zeta \tilde{F}^{n+\frac{1}{2}} \\ \sum_\zeta w_\zeta \tilde{F}^{n+\frac{1}{2}} \end{bmatrix} \\
&+\Delta t \Upsilon \begin{bmatrix} \frac{1}{3}\sum_i w_i |J(\zeta_j)| \left(\frac{1}{2}(F_x)_i^n + \frac{1}{2}(F_x)_i^{n+\frac{1}{3}} \right) \\ \frac{1}{3}\sum_i w_i |J(\zeta_j)| \left(\frac{1}{2}(F_x)_i^n + \frac{1}{2}(F_x)_i^{n+\frac{1}{3}} \right) \\ \sum_i w_i |J(\zeta_j)| \left(\frac{3}{4}(F_y)_i^{n+\frac{1}{3}} + \frac{1}{4}(F_y)_i^{n+1} \right) \\ \sum_i w_i |J(\zeta_j)| \left(\frac{3}{4}(F_y)_i^{n+\frac{1}{3}} + \frac{1}{4}(F_y)_i^{n+1} \right) \end{bmatrix} \\
&+\Delta t \begin{bmatrix} \frac{5}{12} I & -\frac{1}{12} \\ \frac{3}{4} I & \frac{1}{4} \end{bmatrix} \begin{bmatrix} \overline{\frac{\partial S}{\partial U}}^{n+\frac{1}{3}} \Delta_x U_k^{n+\frac{1}{3}} \\ \overline{\frac{\partial S}{\partial U}}^{n+\frac{1}{3}} \Delta_y U_k^{n+\frac{1}{3}} \\ \overline{\frac{\partial S}{\partial U}}^{n+1} \Delta_x U_k^{n+1} \\ \overline{\frac{\partial S}{\partial U}}^{n+1} \Delta_y U_k^{n+1} \end{bmatrix}.
\end{aligned} \tag{3.38}$$

Where I is the identity matrix and Υ is the matrix

$$\Upsilon = \begin{bmatrix} K_k & 0 \\ 0 & K_k \end{bmatrix}. \tag{3.39}$$

3.2 Computation of Intercell Fluxes

The DGH scheme requires the computation of intercell fluxes. This brief section outlines the Riemann problem and HLL approximate Riemann solver.

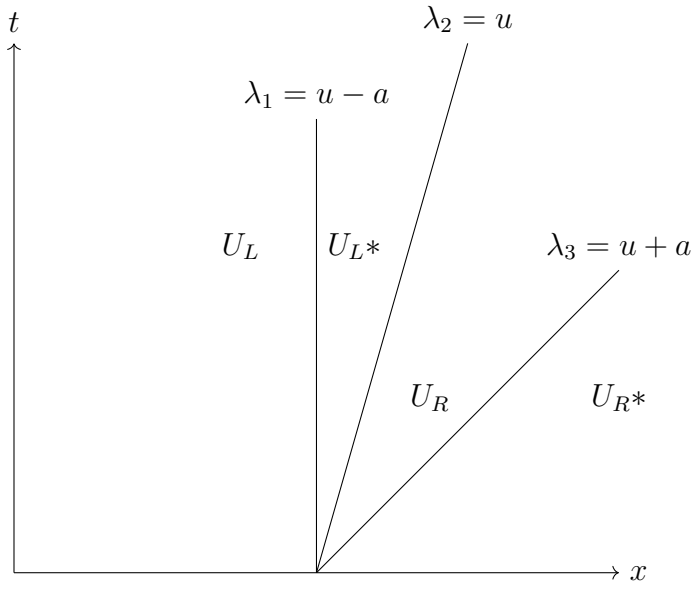

Figure 3.4: One-dimensional illustration of the Riemann Problem.

3.2.1 The Riemann Problem

The Riemann problem is an initial-value problem for a set of conservation equations with piecewise initial conditions. An example of a Riemann problem is seen in Figure 3.4. The case for a one-dimensional system of conservation laws is given by

$$\frac{\partial U}{\partial t} + \frac{\partial F}{\partial x} = 0\,. \tag{3.40}$$

The piecewise initial conditions take the form

$$U(x,0) = \begin{cases} U_L, \text{if } x < 0 \\ \\ U_R, \text{if } x > 0 \end{cases}\,. \tag{3.41}$$

with a discontinuity at $x = 0$. The left state is U_L, and U_R is the right state.

The HLL approximate Riemann Solver

Harten, Lax and van Leer [14] produced an approximate Riemann solver known as HLL. The approximate Riemann solver is popular for complex hyperbolic systems of PDEs, as it only requires knowledge of the fastest left-hand and right-hand wave speeds. The form of HLL can be found by integrating the Eq. (3.40) along

space and time into the form:

$$\iint_S \left[\frac{\partial U}{\partial t} + \frac{\partial F}{\partial x}\right] \mathrm{d}x\mathrm{d}t = 0 \tag{3.42}$$

Greens theorem transforms the integral in Eq. (3.42) into a path integral along the surface of the space-time domain into the form

$$\oint_S (U\mathrm{d}x - F\mathrm{d}t) = 0\,. \tag{3.43}$$

As shown in Figure 3.5, the two waves propagate at speeds λ^+ and λ^- in opposing directions with a state U_m in between each wave. Where λ^+ and λ^- are the largest wave speeds within the solution to the Riemann problem. After a singular time step elapses, the left and right waves will have travelled a distance of $\lambda^+\Delta t$ and $\lambda^-\Delta t$. Evaluating the path integral in Eq (3.43) gives the following form

$$-U_L\lambda^-\Delta t + U_R\lambda^+\Delta t - U_m(\lambda^+ - \lambda^-)\Delta t + F_L\Delta t - F_R\Delta t = 0 \tag{3.44}$$

Both the flux vectors, F_L and F_R, are evaluated at the left and right sides of the discontinuity. Rearranging for U_m produces

$$U_m = \frac{U_R\lambda^+ - U_L\lambda^- - (F_R - F_L)}{\lambda^+ - \lambda^-} \tag{3.45}$$

Determining the Flux, F_m, at $x = 0$ is not as simple as using $F_m = F(U_m)$. This will not satisfy the Rankine-Hugoniot condition, $\Delta F = \lambda\Delta U$. A second path integral can be evaluated on either the left or right side of the discontinuity $x = 0$. The right path integral takes the form:

$$U_R\lambda^+\Delta t - U_m\lambda^+\Delta t - F_R\Delta t + F_m\Delta t = 0. \tag{3.46}$$

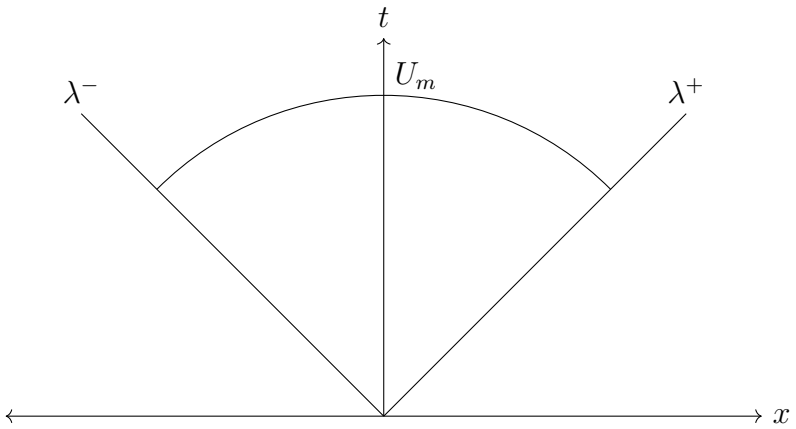

Figure 3.5: Two waves propagate in opposite directions with a state U_m in between

Rearranging to find F_m gives the result,

$$F_m = F_R + \lambda^+(U_m - U_R). \tag{3.47}$$

Finally, substituting Eq (3.45) produces

$$F_m = \frac{\lambda^+ F_L - \lambda^- F_R + \lambda^+\lambda^-(U_R - U_L)}{\lambda^+ - \lambda^-}. \tag{3.48}$$

The final HLL flux function is

$$F = \begin{cases} F_L, \text{ if } \lambda^- > 0 \\ F_m, \text{ if } \lambda^- < 0 \text{ and } \lambda^+ > 0 \\ F_R, \text{ if } \lambda^+ < 0 \end{cases} . \tag{3.49}$$

Newton's Method for Stiff Source Term

The source term in this model is defined by the difference in the Gibbs free energies, g, between two phases multiplied by the density ρ and a relaxation parameter ν. The source takes the following form

$$S = \rho\nu(g_2 - g_1)\,. \tag{3.50}$$

The relaxation parameter ν is assumed to be infinitely large in Saurel's original model [27], thus guaranteeing that the phases reach thermodynamic equilibrium at the saturation conditions instantaneously. This is justified for cavitating flow because it is assumed that the fluids contain many nucleation sites. Nucleation sites are the starting points of phase transition, and the more starting points result in a faster phase transition. The resulting evaporating interface quickly allows for large mass and heat exchange, which necessitates a stiff relaxation source term. When the fluid is pure liquid or gas, the relaxation parameter ν is effectively zero because no phase change occurs. The solution corresponds to thermodynamic equilibrium and is obtained considering the mixture mass and mixture energy definitions:

$$v = \frac{1}{\rho} = Y_1 v_1 + Y_2 v_2 = \text{constant}\,. \tag{3.51}$$

$$e = Y_1 e_1 + Y_2 e_2 = \text{constant}\,. \tag{3.52}$$

This method requires the use of Newton's method to solve the discrete update formulas seen in Eq. (3.37). The update formulas for the mass fraction of liquid, Y_1, take the form

$$\begin{bmatrix} {Y_1}_k^{n+\frac{1}{3}} \\ {Y_1}_k^{n+1} \end{bmatrix} = \begin{bmatrix} {Y_1}_k^{n} \\ {Y_1}_k^{n} \end{bmatrix} - \frac{\Delta t}{A_k} \begin{bmatrix} \frac{1}{3}\sum_\zeta w_\zeta \tilde{F}^{n+\frac{1}{6}} \\ \sum_\zeta w_\zeta \tilde{F}^{n+\frac{1}{2}} \end{bmatrix} + \Delta t \begin{bmatrix} \frac{5}{12}I & -\frac{1}{12} \\ \frac{3}{4}I & \frac{1}{4} \end{bmatrix} \begin{bmatrix} \rho\nu(g_2 - g_1)^{n+\frac{1}{3}} \\ \rho\nu(g_2 - g_1)^{n+1} \end{bmatrix}. \tag{3.53}$$

This can be further simplified by grouping the solution at the current time step and the flux into a term called $\hat{Y}_1$.

$$\begin{bmatrix} {Y_1}^{n+\frac{1}{3}} \\ {Y_1}^{n+1} \end{bmatrix} = \begin{bmatrix} \hat{Y}_1^{n+\frac{1}{6}} \\ \hat{Y}_1^{n+\frac{1}{2}} \end{bmatrix} + \Delta t \begin{bmatrix} \frac{5}{12}I & -\frac{1}{12} \\ \frac{3}{4}I & \frac{1}{4} \end{bmatrix} \begin{bmatrix} \rho\nu(g_2 - g_1)^{n+\frac{1}{3}} \\ \rho\nu(g_2 - g_1)^{n+1} \end{bmatrix}. \tag{3.54}$$

The above equation can be rearranged to produce a function in which the roots are sought,

$$\begin{bmatrix} f_{n+\frac{1}{3}}({Y_1}^{n+\frac{1}{3}}) \\ f_{n+1}({Y_1}^{n+1}) \end{bmatrix} = \begin{bmatrix} \hat{Y_1}^{n+\frac{1}{6}} \\ \hat{Y_1}^{n+\frac{1}{2}} \end{bmatrix} - \begin{bmatrix} {Y_1}^{n+\frac{1}{3}} \\ {Y_1}^{n+1} \end{bmatrix} + \Delta t \begin{bmatrix} \frac{5}{12}I & -\frac{1}{12} \\ \frac{3}{4}I & \frac{1}{4} \end{bmatrix} \begin{bmatrix} \rho\nu(g_2 - g_1)^{n+\frac{1}{3}} \\ \rho\nu(g_2 - g_1)^{n+1} \end{bmatrix}. \tag{3.55}$$

The functions in Eq. (3.55), are functions of the mass fraction of liquid water, Y_1, at time step $t^{n+\frac{1}{3}}$ and t^{n+1}. The energy and density terms are assumed to be constant. The source terms are functions of the gibbs free energy seen in Eq. (2.16), which is a function of temperature and pressure. The temperature and pressure are functions of Y_1 only because energy and density are assumed to be constant. Newton's method is applied to Eq. (3.55) to find the roots of the function. The method iterates over the mass fraction of the liquid Y_1. If Newton's method does not produce a physical solution where Eq. (3.55) is sufficiently close to zero, then the fluid is either a pure liquid or a pure gas.

The form of the function varies depending on the fluid's phase. For example, in Figure 3.6, the function spans $0 \leq Y^{n+1} \leq 1$ and $0 \leq Y^{n+\frac{1}{3}} \leq 1$. The grey area represents the areas in which the function is aphysical. The white line represents the area where the function is zero. The point where both functions are zero is the solution to the problem. In a case where the phases are not within the vapour dome, no intersection occurs, which would mean that the phase is either all liquid or all gas.

3.3 Parallel Computing and Mesh Refinement

The discontinuous-Galerkin-Hancock method was implemented to solve PDEs numerically on modern supercomputers using a large number of CPUs. The PDEs are numerically solved on a structured grid composed of blocks. These blocks are composed of an equal number of cells. Each block is computed on its respective

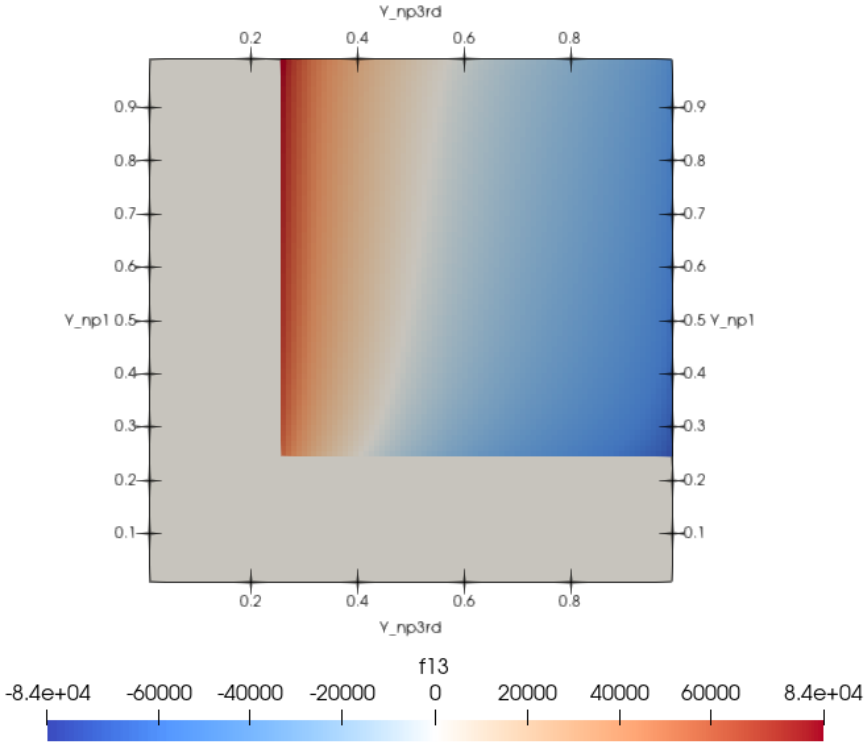

(a) $f_{n+\frac{1}{3}}({Y_1}^{n+\frac{1}{3}}, {Y_1}^{n+1})$

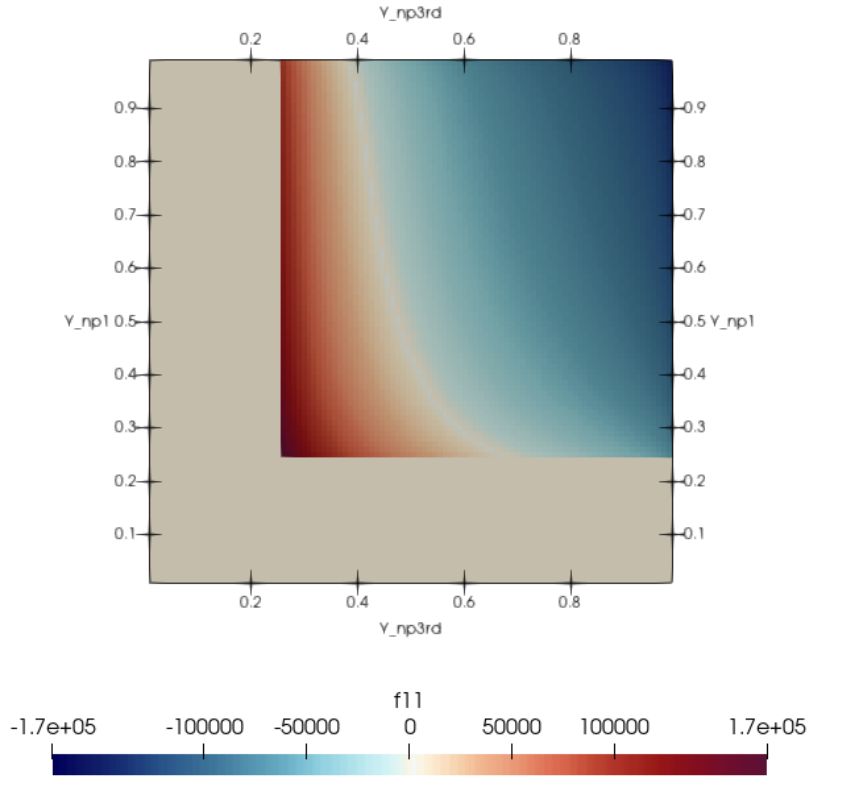

(b) $f_{n+1}({Y_1}^{n+\frac{1}{3}}, {Y_1}^{n+1})$

Figure 3.6: The span of the functions defined in Eq. (3.55).

CPU. The CPUs communicate using a message passing interface (MPI). The C++ library MPI defines message-passing routines between CPU processes. Blocks need to communicate with each other to compute their fluxes and this is facilitated by using MPI.

Mesh Refinement (MR) is a technique that adjusts the accuracy of the simulation. This method can locally increase or decrease the resolution in the mesh. MR can improve the resolution by refining a block, which splits the block into four child blocks. The MR method can reduce the resolution by coarsening the mesh, which combines child blocks into one parent block. A technique known as load balancing is used to distribute the blocks onto the CPUs evenly. Thus, one CPU is not responsible for more computations than any other CPU. All of these blocks have the same number of cells; therefore, guaranteeing a roughly even amount of compute time per CPU.

3.4 Validation

Validation of the model and Noble-Abel stiffened-gas equation of state can be done by computing successive steady-state solutions of the governing PDEs for a range of states in the liquid regime, gaseous regime, and states under the vapour dome to verify agreement with the experimental data. The vapour dome is defined as the range of states for which the vapour quality is neither zero nor one. The vapour quality is defined as the complement of the mass fraction of liquid, Y_{liq}, as shown

$$x = 1 - Y_{liq}\,. \tag{3.56}$$

The thermodynamic state postulate says that any thermodynamic variable can be found from two independent state variables. Using Newton's Method, the enthalpy-pressure vapour dome can be computed by finding zeroes in the source term defined in the above model. The resulting vapour dome, shown in Figure 3.7, has pure liquid, represented in black, and pure vapour, represented in yellow. The

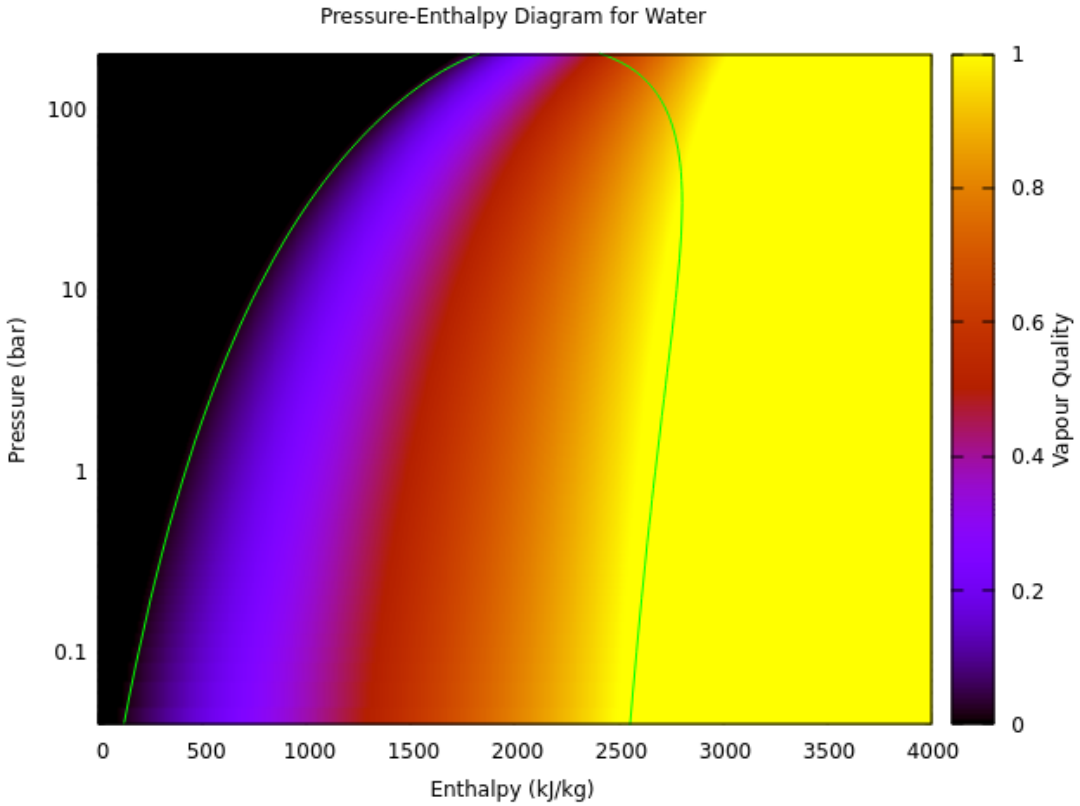

Figure 3.7: The enthalpy-pressure diagram for water with a vapour dome created using Saurel's model.

purple-red spectrum within the vapour dome represents the vapour quality, with purple representing less vapour and more liquid and red representing more vapour and less liquid. The green lines are the outline of the experimentally observed vapour dome. The fit of the Noble-Abel stiffened-gas is not perfect, and near the critical point, the fit diverges from the true enthalpy-pressure vapour dome. This is a well-known deficiency of the Noble-Abel stiffened-gas equation of state [18]. However, lower within the vapour dome, agreement is better. This ultimately validates that the model is suitable to deal with phase transition in the range of states expected in the present application.

Chapter 4

Results

In this Chapter, the numerical results of various simulations are showcased. In Section 4.1, the PDEs and equation of state are validated by simulating classical Riemann problems. In Section 4.2, the discontinuous-Galerkin-Hancock method implementation is verified by comparing the phase transition of a singular cell in time. In Section 4.3, the multiphase model is validated by conducting an investigation of a Venturi nozzle, which exhibits unsteady periodic cavitation. The phase transition model is validated by demonstrating agreement with experimental results. Finally, in Section 4.4, a numeric simulation of the PWJ is shown. An oscillating boundary condition is used to model the motion of the probe, and an axisymmetric treatment is used. A detailed mesh refinement study is carried out to ensure the reliability of numerical solutions. The PWJ is modelled with and without the oscillating probe, and the simulations are compared.

4.1 Verification of Numerical Approximation of PDEs using the Riemann Problem

Riemann problems are used to understand PDEs, such as the one-dimensional Euler conservation equations because shocks and rarefaction waves appear as the characteristics of the solution. This approach allows a comparison between the

simulations and exact solutions of the Riemann problem obtained through the method of characteristics. In the present study, the aim is to demonstrate two objectives: that both the Nobel-Abel stiffened-gas equation of state and mixture conservative Euler equations are correctly implemented in the code. The methodology to simulate Riemann problems is discussed. Then, two Riemann problems using liquid water and water vapour using the DGH scheme are simulated and compared to the analytic solution found using the method of characteristics.

4.1.1 Determination of Exact Solutions

The NASG equation of state can be used to find the various quantities associated with compressible flows, such as the isentrope, sound speed, and the other variables associated with the Riemann problem. Radulescu derived the expressions for the isentrope, sound speed, isentropic exponent, and other Riemann variables, which are ultimately used to solve Riemann problems [24]. The shock jump equation for speed is

$$\frac{u_2 - u_1}{c_1} = \left(1 - \frac{b}{v_1}\right) \frac{2(M_s^2 - 1)}{(\gamma + 1)M_s}, \tag{4.1}$$

with M_s as the shock Mach number. Subscripts 1 and 2 denote the two regions separated by the shock wave. The shock jump equation for the difference in pressure is

$$\frac{\bar{p}_2}{\bar{p}_1} = 1 + \frac{2\gamma(M_s^2 - 1)}{(\gamma + 1)}, \tag{4.2}$$

with $\bar{p} = p + p_\infty$ and the difference in specific volume is

$$\frac{\bar{v}_2}{\bar{v}_1} = \frac{(\gamma - 1)M_s^2 + 2}{(\gamma + 1)M_s^2}, \tag{4.3}$$

with $\bar{v} = v - b$.

The characteristic and the polytropic gas relations are used to solve a left or

Table 4.1: NASG coefficients for liquid water, water vapour, and air in the temperature range [300–500 K].

Coefficients	Liquid water	Water Vapour	Air
γ	1.19	1.47	1.4
P_∞ (Pa)	7.028×10^8	0	0
b (m^3/kg)	6.61×10^-4	0	0
q (J/kg)	-1177 788.0	2 077 616.0	0
q' (J/kg)	0	14 317.0	0
C_p (J/(kg K))	4285.0	1401.0	1004.7
C_p (J/(kg K))	3610.0	955.0	717.6

right rarefaction wave. The characteristic equation takes the form of

$$J_\pm = \sqrt{\gamma(p + P_\infty)(v - b)} \pm u = \text{constant}\,, \tag{4.4}$$

and the polytropic gas relation is

$$(p + P_\infty)(v - b)^\gamma = \text{constant}. \tag{4.5}$$

Characteristic solutions can be found using the shock-jump equations and a method outlined by Gottlieb and Groth [13]. The analytic solution found using the Gottlieb and Groth method is compared to the fluid simulation using the present DGH numerical method. The chosen Riemann problems are of RCS form, which means rarefaction-contact-shock waves. The two mediums are water vapour and liquid water. The values outlined in Table 4.1 for the constants of the Nobel-Abel stiffened-gas equation of state are used.

4.1.2 Water Vapour Riemann Problem Comparative Analysis

The first Riemann problem involves a shock tube of 1.0 m in length filled two media with a constant thermodynamic state separated by a barrier. Both media are water vapour. When the barrier between the left and right regions, seen in

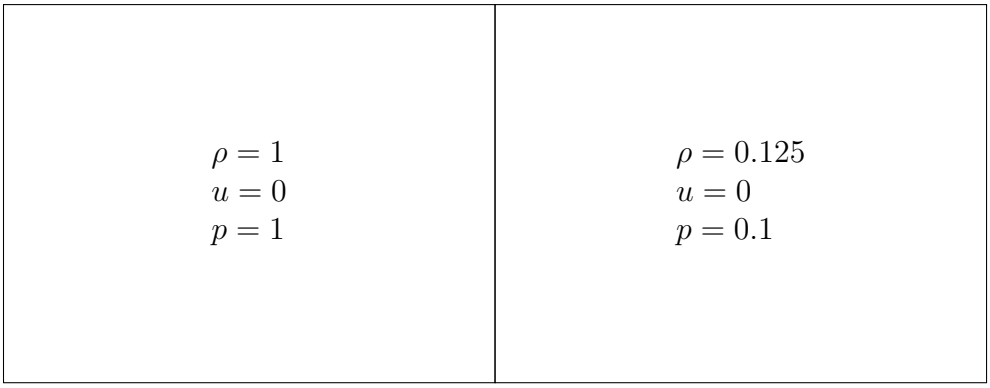

Figure 4.1: Riemann problem for water vapour. The tube length is 1.0 unit length with a discontinuity at $x = 0.5$ unit length.

Figure 4.1, is removed, a shock wave, a contact discontinuity and a rarefaction wave form. The CFL number used is 0.10. The simulation occurs on a 1000 cell mesh. It uses the HLL flux function and Venkatakrishnan slope limiter. It is time-marched to t =0.2

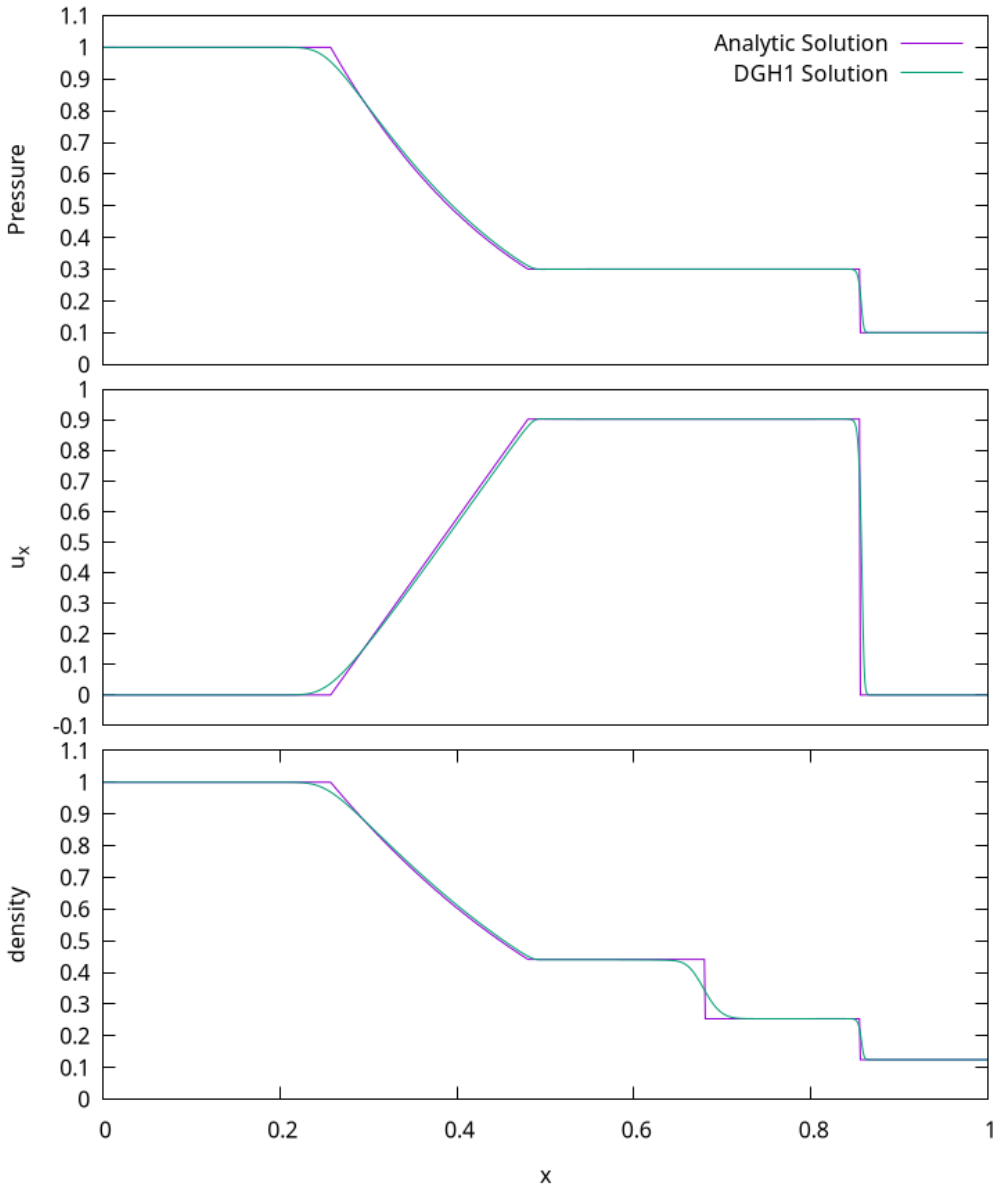

Figure 4.2: Riemann-problem solution for water vapour at time t=0.2

The analytic solution and the DGH method are shown in Figure 4.2 with the pressure, velocity, and density shown. The rarefaction, contact discontinuity and shockwave are seen in these graphs. The solutions are similar, but the DGH solution is more diffuse. If the DGH solution had more cells, it would eventually converge to the analytic solution.

The Nobel-Abel stiffened-gas equation of state acts very similarly to a perfect gas. This is because the Noble-Abel Stiffened-gas equation of state simplifies to an equation that takes the form of the perfect gas equation of state when modelling

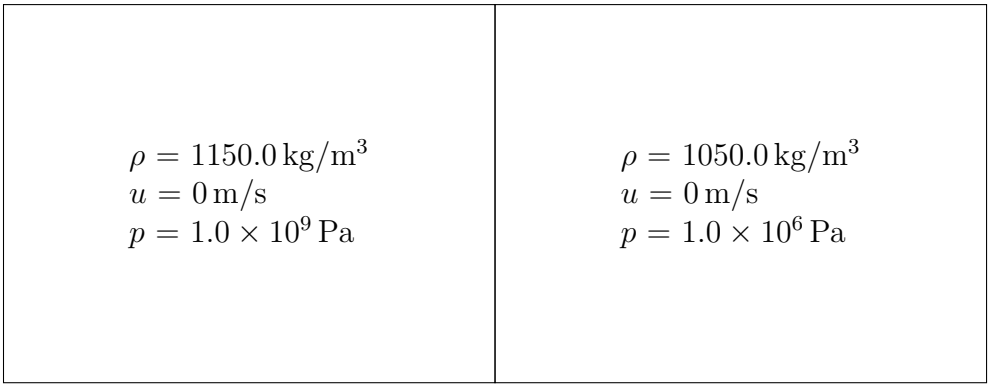

Figure 4.3: Riemann problem for liquid water. The length of the tube is One unit length with a discontinuity at $x = 0.5\,\mathrm{m}$.

a fluid that is pure gas, as shown in the following equation:

$$P = (\gamma - 1)\frac{e - q}{v - b} - \gamma P_\infty \rightarrow P = (\gamma - 1)\frac{e - q}{v}\,. \tag{4.6}$$

This is due to the fact that the NASG coefficients for P_∞ and b are zero for gaseous fluids.

4.1.3 Liquid Water Riemann Problem Comparative Analysis

The same scenario is also studied for liquid water with a shock tube of 1m in length that contains two regions of differing density and pressure separated by a barrier, which is removed as can be seen in Figure 4.3. The CFL number used is 0.10. The simulation occurs on a 1000 cell mesh. It uses the HLL flux function and Venkatakrishnan slope limiter. It is time-marched to $t = 75.0 \times 10^{-6}\,\mathrm{s}$. Figure 4.2 shows the pressure, velocity, and density plots with the analytic and DGH solutions. The rarefaction, contact line, and shockwave are seen in these graphs. The rigidity of liquid water can be seen as the wave speeds are much faster, with the solution end time at $75.0 \times 10^{-6}\,\mathrm{s}$. The solutions of the analytic and DGH scheme are very similar.

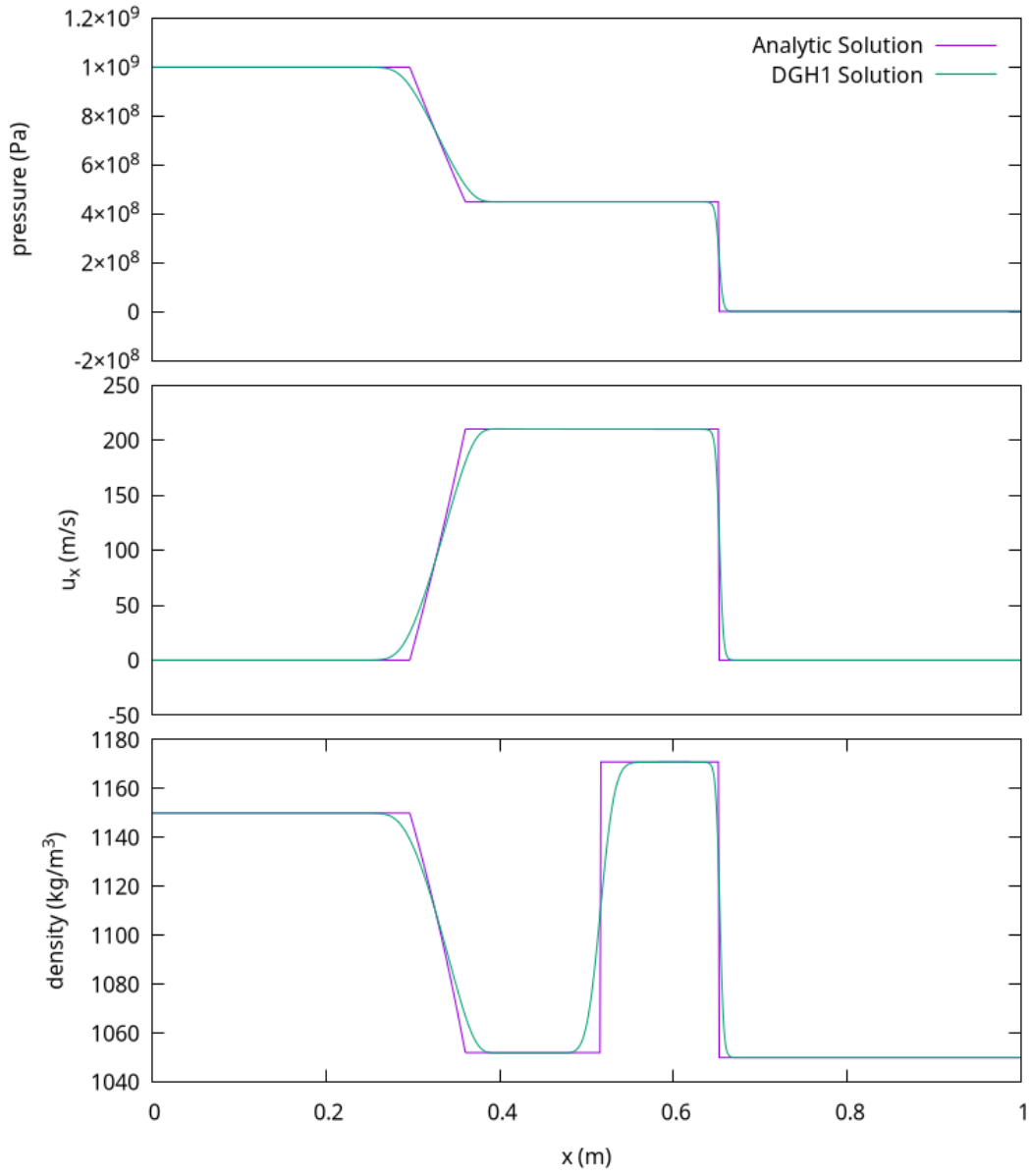

Figure 4.4: Riemann-problem solution for liquid water at time $t = 75.0 \times 10^{-6}$ s.

4.1.4 Conclusion

This study has verified the implementation of the NASG EOS and the mixture Euler PDEs can numerically solve Riemann problems accurately, as predicted in the review of the various models of equations of states. The results give confidence that the code is implemented correctly and can be used to study realistic cases.

4.2 Verification of the Source Term Implementation

Another method of validating the phase transition model is to compare the explicit treatment of the source term, the implicit Euler, and the Radau-IIA method. This allows for an understanding of how the rate of the phase of transition is affected by the stiff relaxation parameter, ν, and verification that Newton's method solver is correctly implemented for the discontinuous-Galerkin method.

4.2.1 Methodology

The methodology used here is to take a fluid that is in the process of transitioning from one state to another within the saturation dome. The chosen initial state is $\rho = 1000\,\mathrm{kg/m^3}$, $Y_{liq} = 0.75$, $e_{liq} = 313.90 \times 10^3\,\mathrm{J}$, $e_{vap} = 2475.9 \times 10^3\,\mathrm{J}$, and $e = 0.9e_{liq} + 0.1e_{vap} = 530.1 \times 10^3\,\mathrm{J}$. The energy is at a value normally associated with a more condensed liquid mixture than the current state of the fluid. Therefore, there is a mismatch between the mass fraction and the energy, which spurs the phase transition to a more condensed mixture. The domain is taken to be spatially homogeneous; thus, there are no flux terms, and the solution evolves based only on the source term.

The value of ν cannot be considered infinite in computation. Thus, a sufficiently large value for the relaxation parameter of $1.0 \times 10^{40}\,\mathrm{m^3/J}$ is used. The value of ν being a real number allows for plotting the mass fraction against time because the phase transition is not instantaneous. This allows for a comparison of the accuracy of the phase-transition rates of each method. The final time is $9 \times 10^{-47}\,\mathrm{s}$ and 1000 time steps are taken where the time step, $\mathrm{d}t$, is $9 \times 10^{-50}\,\mathrm{s}$.

The explicit source time marching is a simple calculation in the form of

$$U(t^{n+1}) = U(t^n) + \Delta t S(U(t^n))\,. \tag{4.7}$$

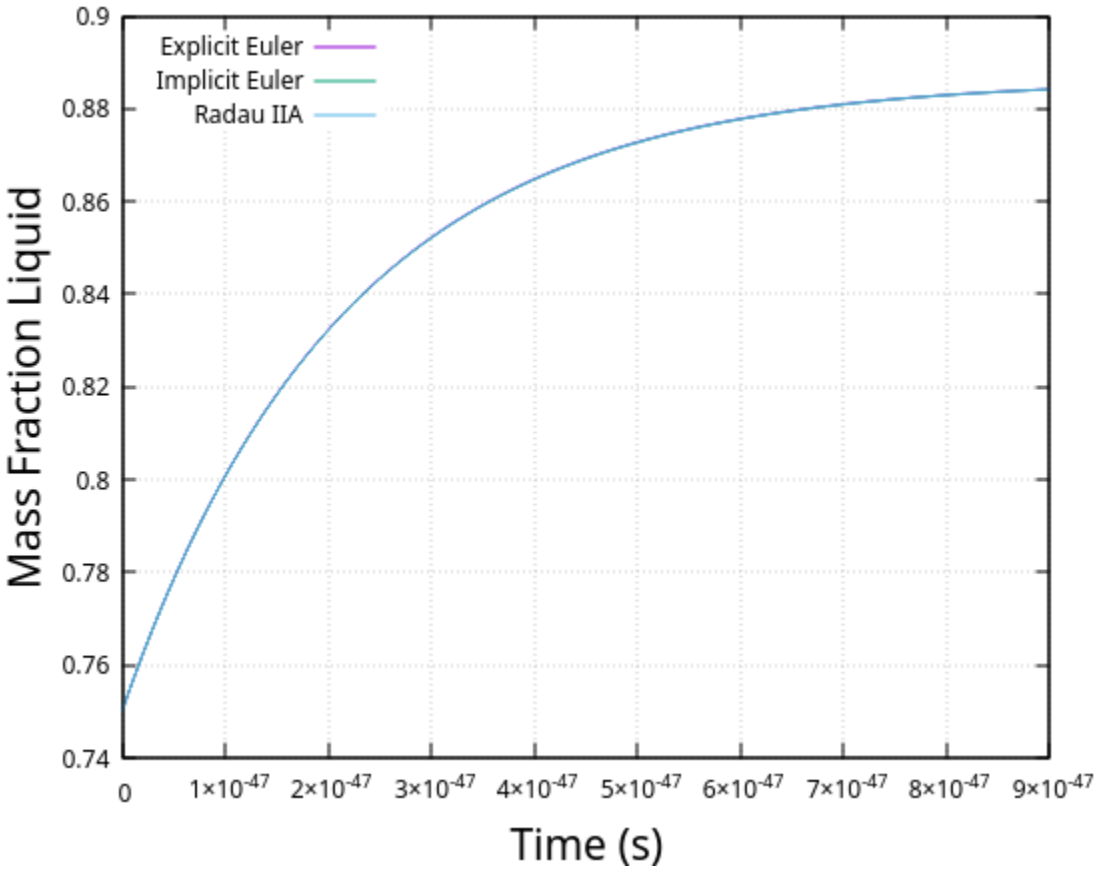

Figure 4.5: The comparison of the explicit treatment of the source term, the implicit Euler and the Radau-IIA method outlined in discontinuous-Galerkin-Hancock method solution.

Where U is the solution vector, and S is the source vector. The Radau-IIA method is outlined in this thesis, and the implicit Euler is a first-order scheme.

4.2.2 Discussion

Figure 4.5 shows a mixture smoothly beginning to condense. The explicit treatment of the source term, the implicit Euler method and the Radau-IIA method are all on top of each other in the figure, which means that the discontinuous-Galerkin-Hancock method is implemented correctly because the solutions agree. The time scale is also extremely small; thus, it is safe to assume that using a ν of this value is sufficiently large.

4.3 Unsteady Cavitation in a Venturi Nozzle

This portion of the study examines a 8° venturi nozzle, which exhibits unsteady cavitation. The venturi nozzle has a converging section at 18° and a diverging section at an angle of 8°. In experimental settings within this converging-diverging section, a periodic flow is observed with a cavitation pocket appearing and then shedding a portion of the cavitation pocket that moves along the flow. The venturi nozzle was built at the LEGI laboratory in Grenoble, France, to study unsteady cavitation typical of turbomachinery [11].

This study aims to validate the phase transition within Saurel's model using this simulation, which has a cavitating region. The 8° venturi nozzle is a much more complex flow than a Riemann problem, which is one-dimensional. This simulation also allows further validation of the PDEs and further verification of the numerics and equation of state. The methodology, refinement study, and a comparison to the experimental venturi are presented in the following section.

4.3.1 Simulation Parameters and Boundary Conditions

The constants used are those in Table 4.1. The geometry of the venturi nozzle can be seen in Figure 4.6 with the values of each point found in Table 4.2. The flow moves from the left of the nozzle to the right, creating an unsteady cavitation bubble. The simulation was time marched for 1.8 s. Saurel also used this case to validate his model [27]. It should also be noted that Saurel used a low Mach number preconditioner because of convergence issues at low Mach numbers. This is due to the compressible Navier-Stokes equations becoming stiff because of a large speed of sound, but small fluid flow velocities. This preconditioner is unnecessary to help with convergence when using the DGH scheme because of its third-order accuracy, and low numerical dissipation..

Initial Fluid Properties: The simulation has both vapour and liquid phases. The initial density of water is $\rho_{liq} = 1067.56\,\mathrm{kg/m^3}$, and the initial density of

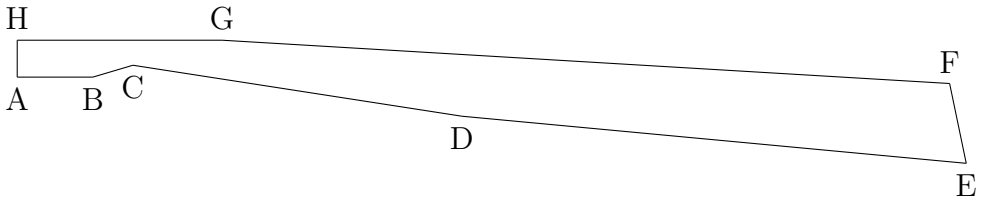

Figure 4.6: The geometry of the Venturi 8° nozzle.

Table 4.2: Vertex coordinates for the venturi nozzle.

Vertex	x-coordinate(m)	y-coordinate (m)
A	0	0
B	0.1	0
C	0.153	0.0157
D	0.588	-0.0517
E	1.225	-0.114
F	1.233	-0.00845
G	0.271	0.0488
H	0.0	0.0488

vapour is $\rho_{vap} = 0.387\,\mathrm{kg/m^3}$. The initial value of the volume fraction of the liquid is $\alpha_{liq} = 0.999$

Boundary Conditions

The boundary conditions in this section are detailed, which are the same as Saurel's simulation [27].

Inlet: The inlet boundary condition is constant mass flow is $\dot{m} = 7514.917\,\mathrm{kg/(m^2\,s)}$, and the pressure $P_{inlet} = 51\,825\,\mathrm{Pa}$.

Outlet: The outlet boundary condition is constant pressure at $P_{outlet} = 72\,025.0\,\mathrm{Pa}$.

Walls: The walls are the reflection boundary condition.

4.3.2 Refinement Study

A mesh refinement study was conducted to model this flow phenomenon accurately. To compute this unstable flow, a two-dimensional structured mesh was employed along with the DGH scheme and the HLL approximate Riemann solver [14]. The slope limiter used was Venkatakrishnan [34]. A visual test is used to

assess the convergence of the numerical results and, therefore, can only measure the sensitivity of the solution to mesh refinement through non-objective methods. As seen in Figure 4.7, the simulation domain is large compared to the area of interest where the cavitation occurs. Therefore, a majority of the refinement occurs at the choke point C, where the quasi-periodic cavitation shedding occurs. A CFL number of 0.45 is used. Each mesh tested is composed of blocks, which themselves are comprised of 50 by 25 quadrilateral cells.

The first mesh, in Figure 4.8, has 42 blocks and a total of 52 500 cells, the second mesh, in Figure 4.9, has 138 blocks and a total of 172 500 cells, and the final study, in Figure 4.10, has 330 blocks and a total of 412 500 cells. The void fraction is used as a way to assess the quality of the mesh.

Coarsest Mesh: In Figure 4.8, this mesh is the coarsest and does not exhibit quasi-periodic vortex shedding but still has a vapour bubble form.

Refined Mesh: In Figure 4.9, the mesh is further refined in the cavitation region, and after refinement, it displays a quasi-periodic cavitation bubble.

Most Refined Mesh: In Figure 4.10, the mesh undergoes a last refinement in the area where it is cavitating. This mesh produces the best quasi-periodic shedding that is most similar to the cavitation described by Saurel in [27].

4.3.3 Discussion

The periodic flow cycle that is observed within the 8° Venturi nozzle has five stages as can be seen Figure 4.13, which is the simulation, and Figure 4.12, which is the experimental:

1. A cavitation sheet forms after the diverging section as seen in Figure 4.13a and reaches a maximum size as seen in Figure 4.13b

2. After reaching a maximum size, the cavitation bubble breaks into two portions, seen in Figure 4.13c.

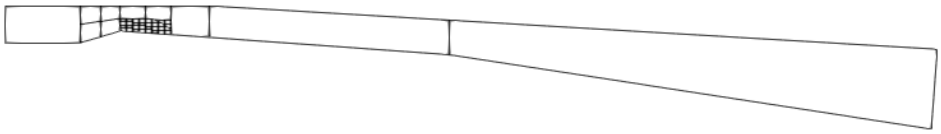

(a) The blocks of the venturi nozzle.

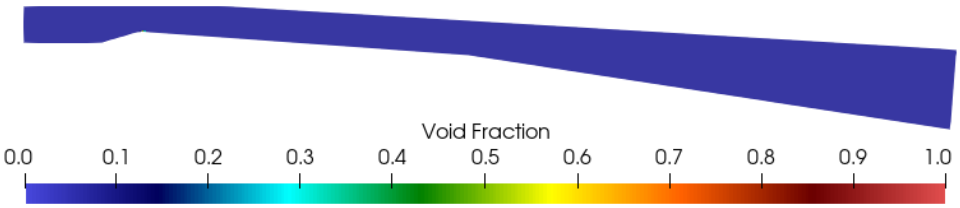

(b) Domain

Figure 4.7: The top picture is the venturi nozzle mesh, and the bottom is the void fraction. As seen above in the bottom image, a majority of the domain is steady. Only near the throat of the venturi does the quasi-periodic cavitation shedding occur.

3. The downstream portion is swept down the flow, and the cavitation bubbles begin to collapse, as seen in Figure 4.13d.

4. The cycle begins again with a quasi-periodic vapour cloud shedding frequency that is 45 Hz and an average sheet cavity length of (45.0 ± 0.5) mm. In the simulation, the maximum length is 54 mm, and the minimum is 40 mm. Thus, this would be a (47.0 ± 0.7) mm. The frequency is close to a range of 40 Hz to 45 Hz.

As seen in Figure 4.11, the difference in Gibbs free energy is zero within the vapour bubbles seen in Figure 4.10. The pressure also descends below the vapour pressure of 2300 Pa. This shows that the vapour bubble is formed from the low pressure, creating an equality in the Gibbs free energies of vapour and liquid. The Newton's Method solver finds this equality as described in Chapter 3.

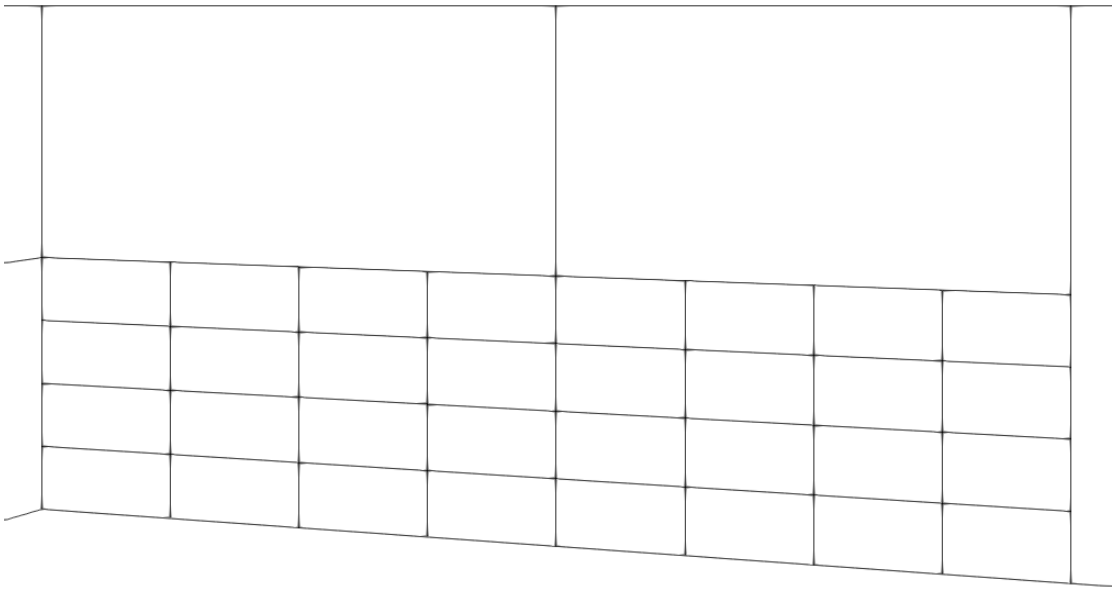

(a) The blocks of the venturi nozzle.

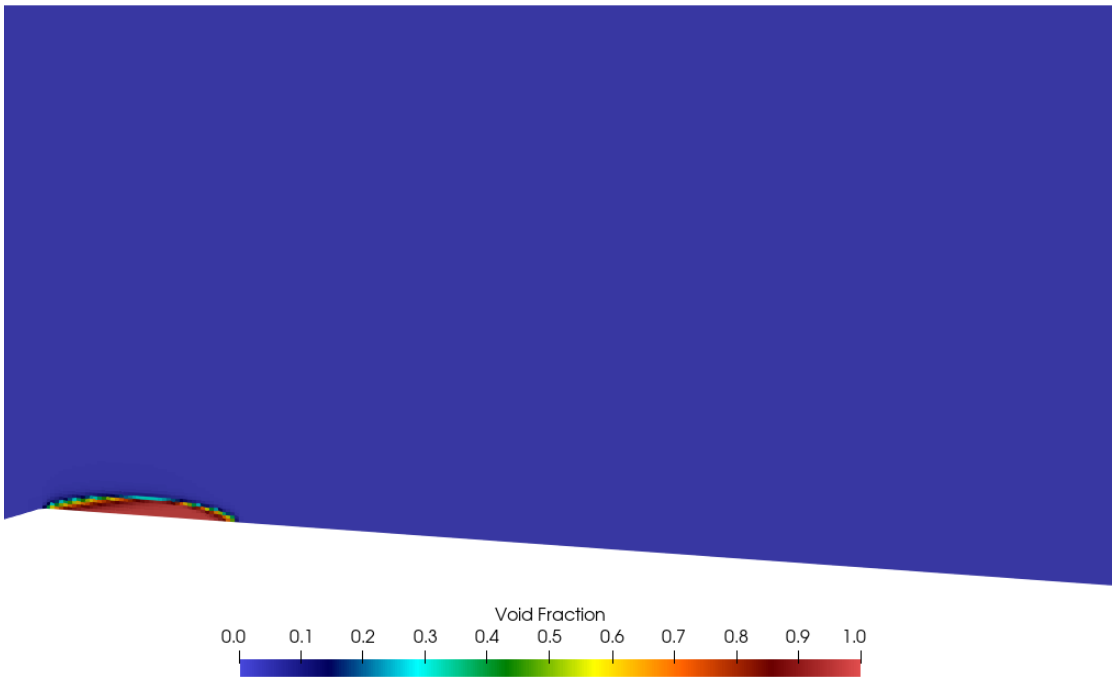

(b) Domain

Figure 4.8: This is a fluid simulation that ran on 42 blocks, each composed of 50 by 25 quadrilateral cells. This simulation ran for $t = 1.8\,\mathrm{s}$. This possessed a cavitation bubble but did not have quasi-periodic shedding.

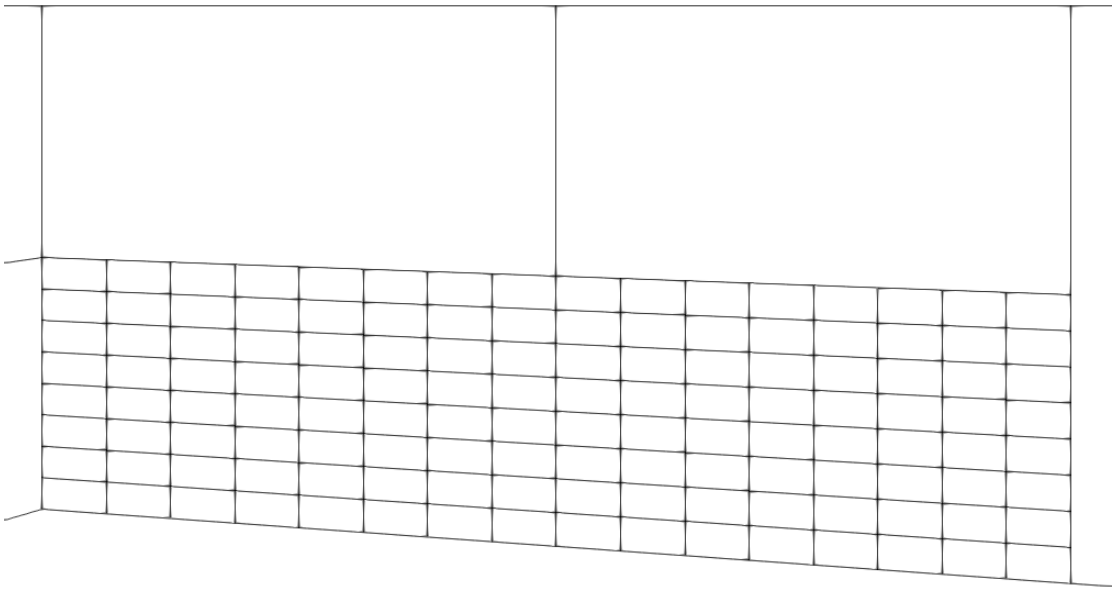

(a) The blocks of the venturi nozzle.

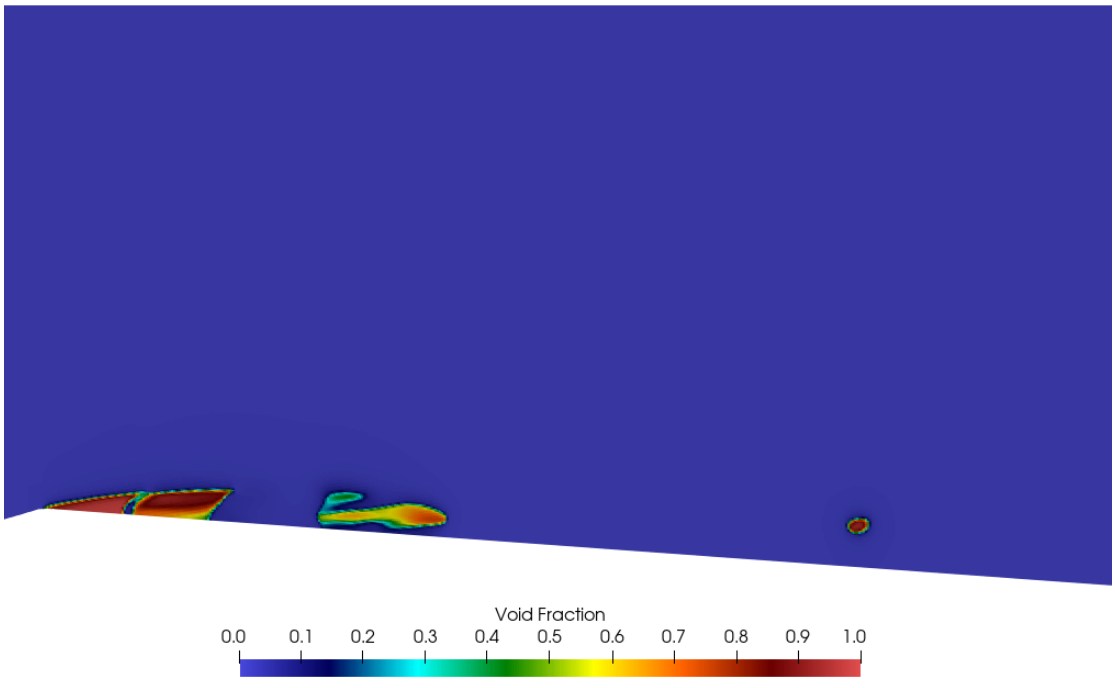

(b) Domain

Figure 4.9: This is a fluid simulation that ran on 138 blocks, each composed of 50 by 25 quadrilateral cells. This simulation ran for $t = 1.8\,\mathrm{s}$. This possessed a cavitation bubble with quasi-periodic shedding.

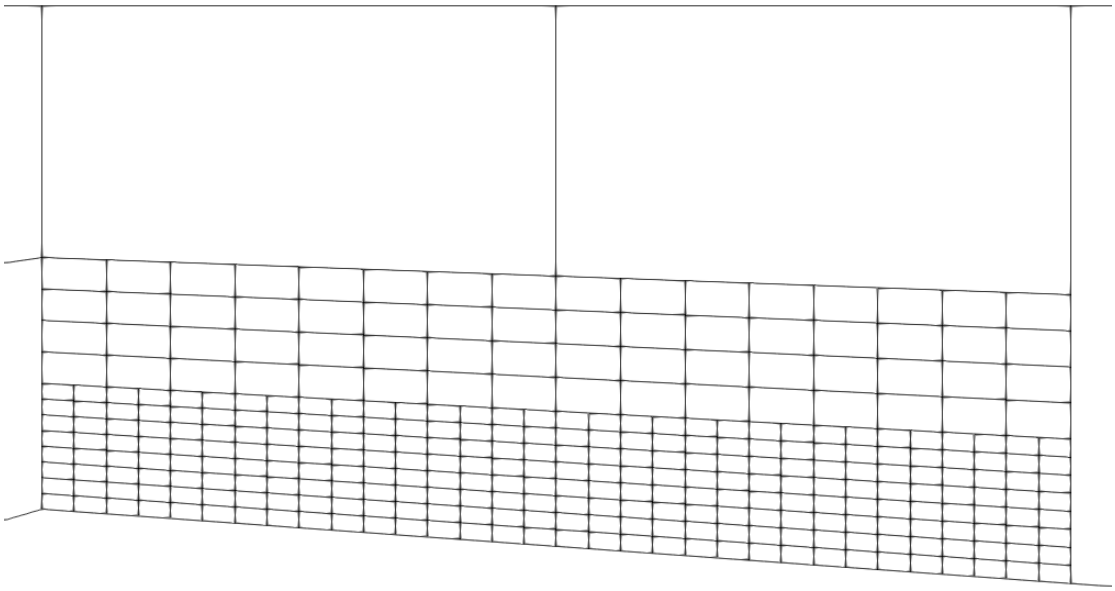

(a) The blocks of the venturi nozzle.

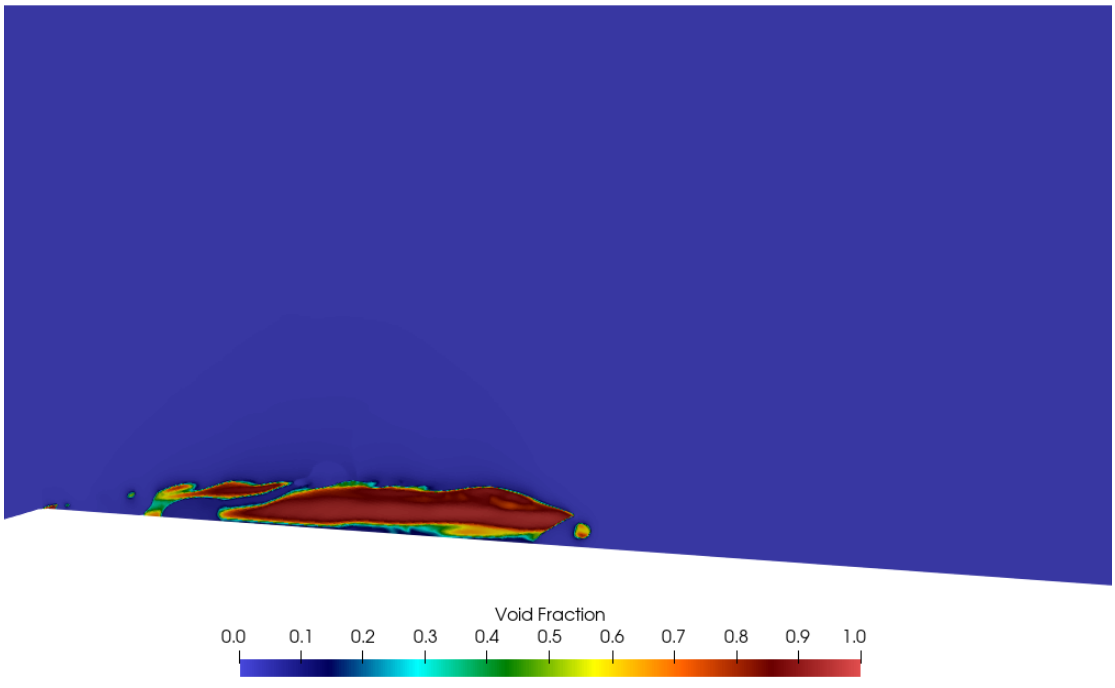

(b) Domain

Figure 4.10: This is a fluid simulation that ran on 330 blocks, each composed of 50 by 25 quadrilateral cells. This simulation ran for $t = 1.8\,\mathrm{s}$. This possessed a cavitation bubble with quasi-periodic shedding

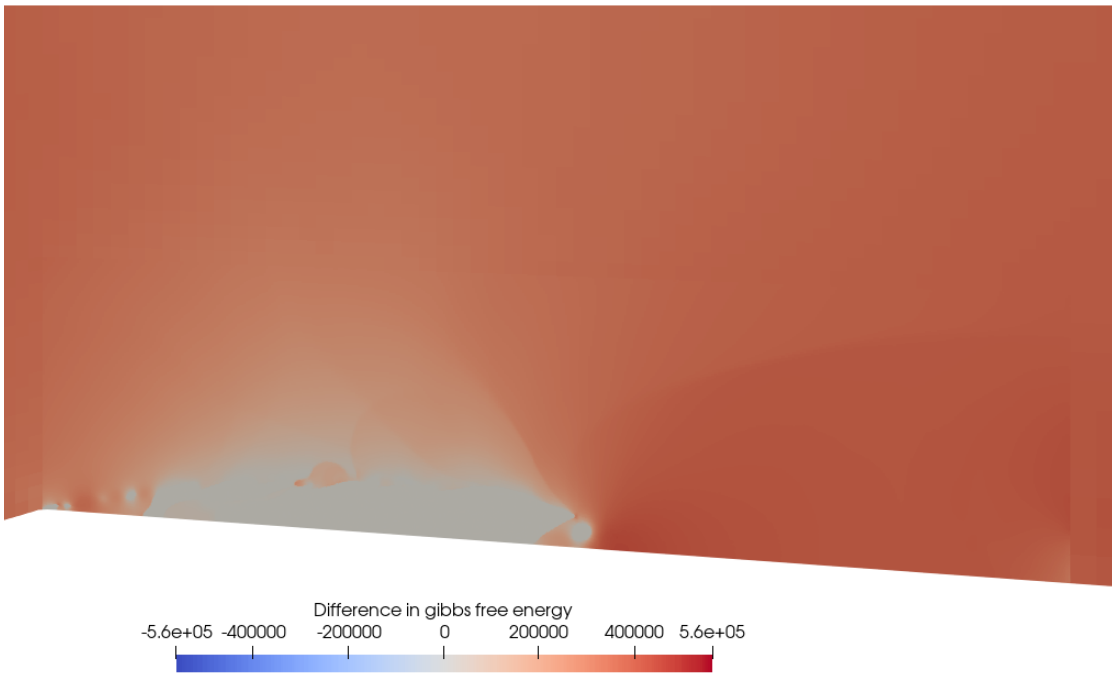

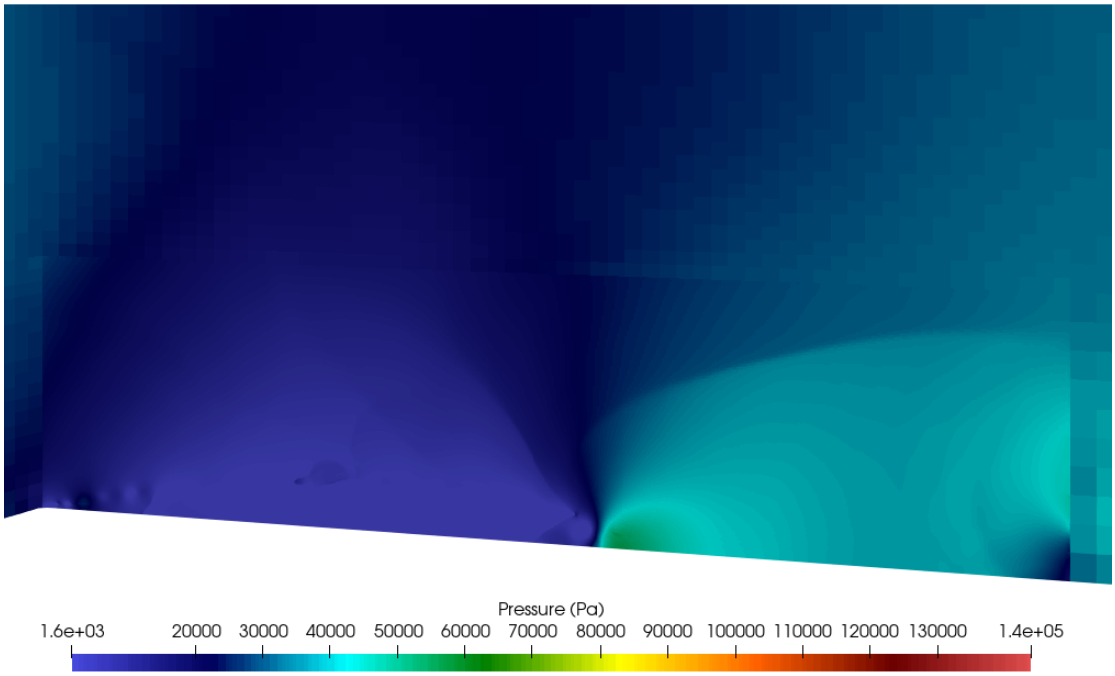

Figure 4.11: The top image is the difference in Gibbs's free energy field, and the second image is the pressure field. Both of these images take the form of a vapour bubble.

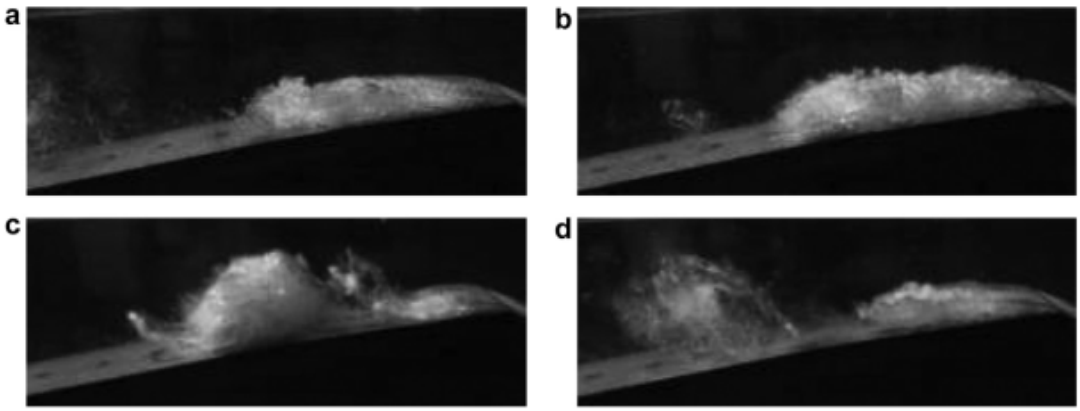

Figure 4.12: Experimental photographs taken from Saurel [27] of the quasi-periodic cavitation shedding cycle in the 8° Venturi nozzle. A. Cavitation pocket appears. B. The cavitation pocket extends and separates into two sub-pockets. C. One vapour packet is transported with the mean flow. D. Another vapour pocket collapses close to the nozzle [27].

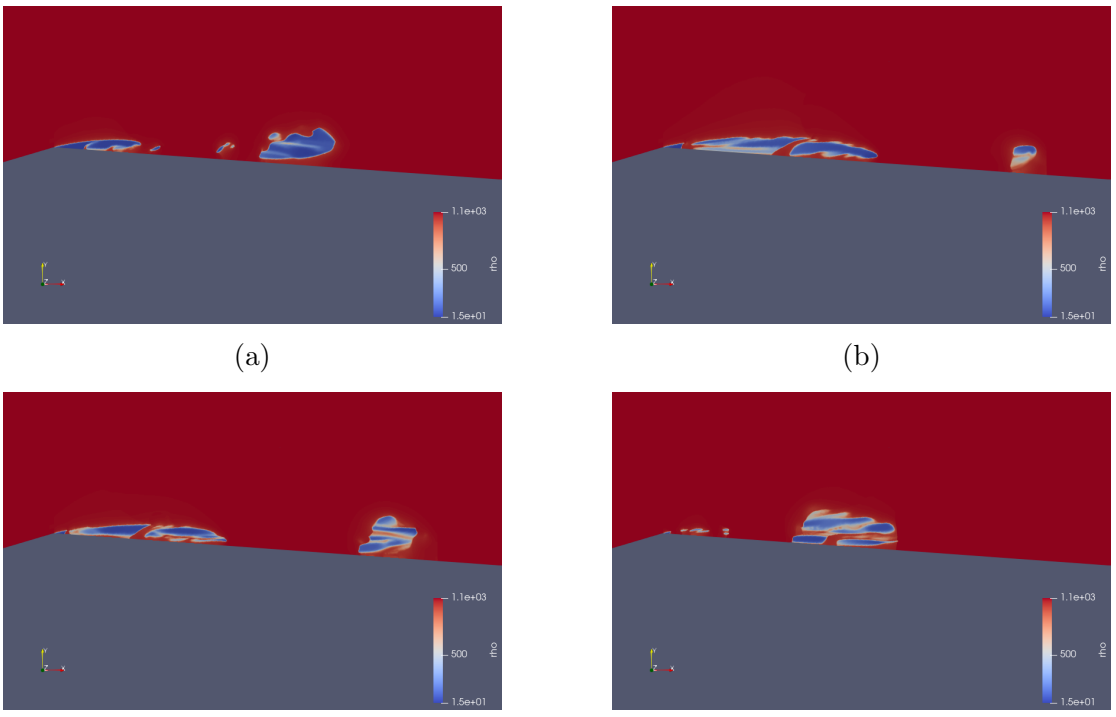

(a) (b)

(c) (d)

Figure 4.13: Simulation of the quasi-periodic cavitation shedding cycle in the 8° Venturi nozzle. A. Cavitation pocket appears. B. The cavitation pocket extends and separates into two sub-pockets. C. One vapour packet is transported with the mean flow. D. Another vapour pocket collapses close to the nozzle.

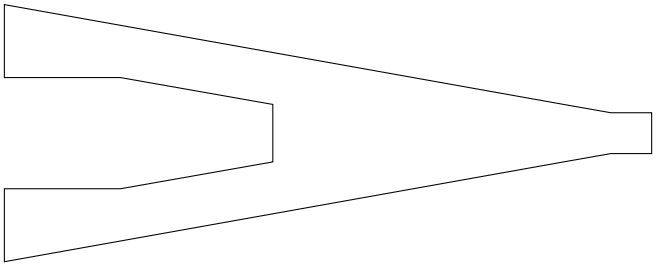

Figure 4.14: The cross-section of the conical PWJ.

4.3.4 Conclusion

These results show that it is possible to use the DGH method along with the Noble-Abel stiffened-gas equation of state to recreate complex cavitation phenomenon.

4.4 Pulsed Waterjet

In this section, the PWJ simulation is discussed. The main goal is to study the physics of the process within the PWJ nozzle, the form of the jet in the air, and its characteristics as it hits the wall. There are two distinct simulations, one of the nozzles without the oscillating probe and another with the oscillating probe boundary condition turned on. The emphasis of this study is on how the oscillating probe alters the flow of the jet. The flow characteristics, such as the velocity, pressure, and density, are studied.

4.4.1 Domain and Boundary Conditions

The PWJ is axisymmetric, as seen in the cross-section in Figure 4.14. The nozzle is conical and the probe is placed within it. The high-frequency oscillations of the probe cause pressure waves to rebound throughout the nozzle.

Boundary Conditions

To simulate the PWJ effectively, the correct boundary conditions need to be used. The axisymmetric boundary allows the efficient use of computing power. The boundary is used along the x-axis of the simulation domain, as can be seen in

Figure 4.15 and Figure 4.16.

Another important boundary is that of the oscillating probe. Its velocity takes the form of a sinusoid:

$$\vec{u} = 2\pi A f \cos(2\pi f t)\hat{n}\,.$$

Where A is the amplitude of the probe displacement, f is the frequency of the oscillating probe, $\hat{n}$ is the velocity direction, and t is the time. The amplitude of the probe is 75.0 µm, and the frequency is 40 000 Hz. Assuming that the boundary takes the form of a sinusoidal function may not always be the case, as the probe may not always act smoothly. The oscillating probe boundary can be seen in Figure 4.16, where the probe fits within the nozzle. In part 1 of the simulation, the oscillating probe boundary condition is off, and the boundary condition acts like a reflective wall. For part 2 of the simulation, the boundary condition for the oscillating probe is used.

The initial conditions of the simulation are set so that the nozzle shoots liquid water out into the air and hits a reflective wall. The top of the domain is the constant atmospheric pressure boundary condition, with the left and right walls being reflective, as shown in Figure 4.15. Air is assumed to act as a perfect gas, and its properties can be seen in Table 4.1. The inlet condition for the flow assumes a constant mass flow of 0.0352 m^3/min of liquid water and a pressure of 1.03×10^8 Pa. The nozzle walls are reflective.

Refinement Study

A mesh refinement study was conducted to model the PWJ accurately. The flow uses a two-dimensional structured grid, the DGH scheme, and the HLL approximate Riemann solver [14]. The simulation was time marched to 0.003 075 s. Due to difficulties using the DGH with axisymmetric boundary conditions, the simulation is reduced to first-order accuracy. The difficulties arise by calculating the source term at the cell edge. The axisymmetric system in Eq. (2.9) has a $1/r$ term

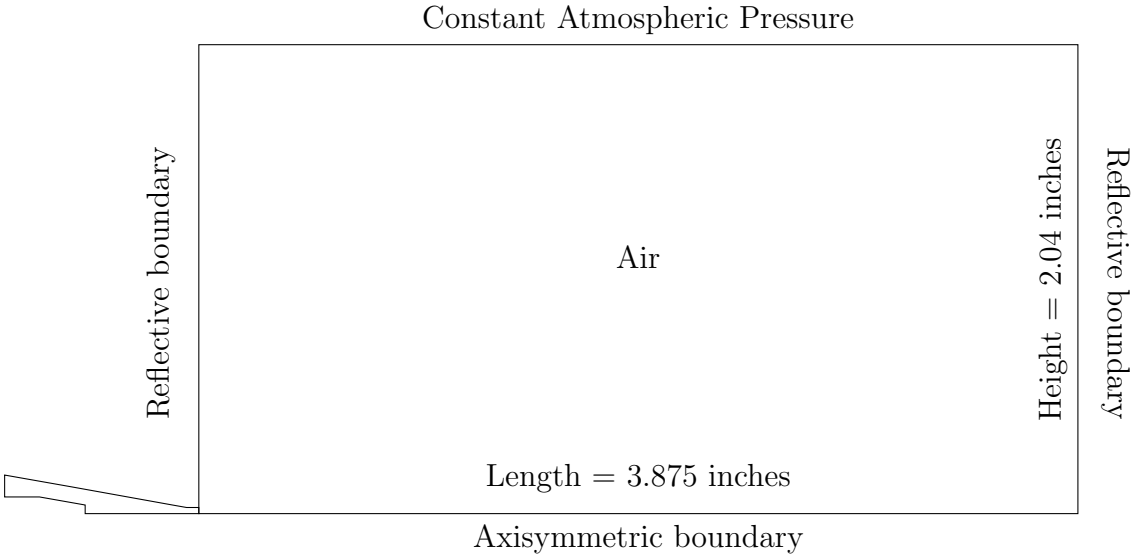

Figure 4.15: The domain of the simulation

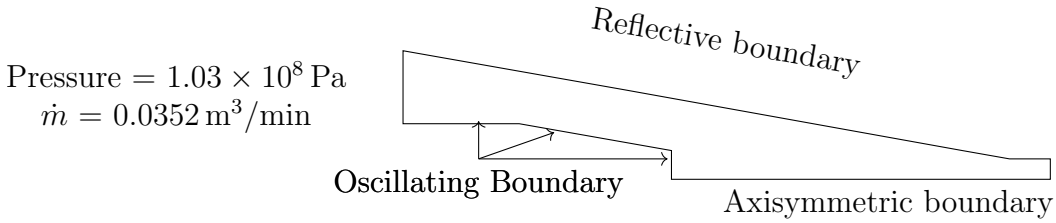

Figure 4.16: The boundary conditions of the PWJ.

in the source term and $r = 0$ at the edge. This produces a division by zero at the cell edge, which is impossible.

The convergence of the simulation is assessed using a visual test, and, therefore, the sensitivity of the solution to mesh refinement is not wholly accurate. A CFL number of 0.8 is used. The first mesh, in Figure 4.17, had 77 blocks and 612 000 cells. In Figure 4.18, the mesh is refined to have 308 blocks and 2 448 000 cells. In Figure 4.19, the final study has 554 blocks and 3 721 500 cells. To compare the meshes, the velocity of the PWJ is used as a test for the solution's accuracy based on the mesh refinement level. The mesh in Figure 4.17 has the coarsest mesh and produces a less focused jet with a slower velocity. Figure 4.18 and Figure 4.19 both have jets of very similar form and velocity, which might indicate that for the current simulation, refining the mesh would not produce a more accurate solution, but the finer mesh in Figure 4.19 is preferred as it is better suited for modelling the pulses produced by the oscillating probe.

4.4.2 PWJ without the probe

The goal of this simulation is to simulate the PWJ without the probe to show the difference between the physics in the jet when the oscillating probe is absent versus when it is present.

Figure 4.20 shows the predicted density field. The density of water at this temperature and pressure of 1.03×10^8 Pa is 1093.0 kg/m^3. Along the jet, as the liquid water interacts more with the air, it begins to mix with the air, as can be seen with the density decreasing. The farther the jet is from its axis of rotation, the more air is entrained within. As the jet's radius increases, the density decreases. Continuous interaction with the water jet and the air results in the break-up of the water jet stream into droplets.

Figure 4.21 shows the pressure field. The PWJ pressure is highest within the nozzle and slowly decays as it reaches the nozzle exit. The pressure on the wall jumps due to the sudden impact of the jet against the wall. This is the water

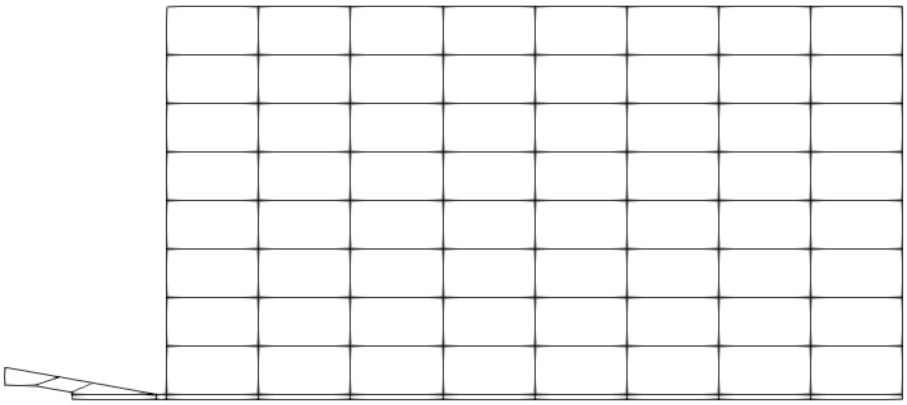

(a) The blocks of the jet simulation.

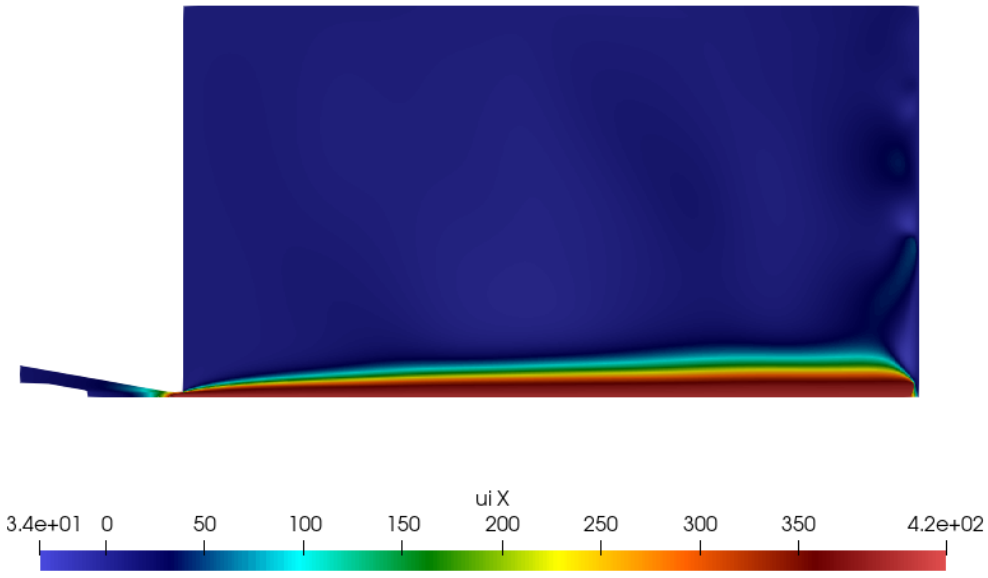

(b) Domain

Figure 4.17: The top image is the mesh of the PWJ, and the bottom is the velocity field in metres per second. This is a PWJ simulation that ran on 77 blocks.

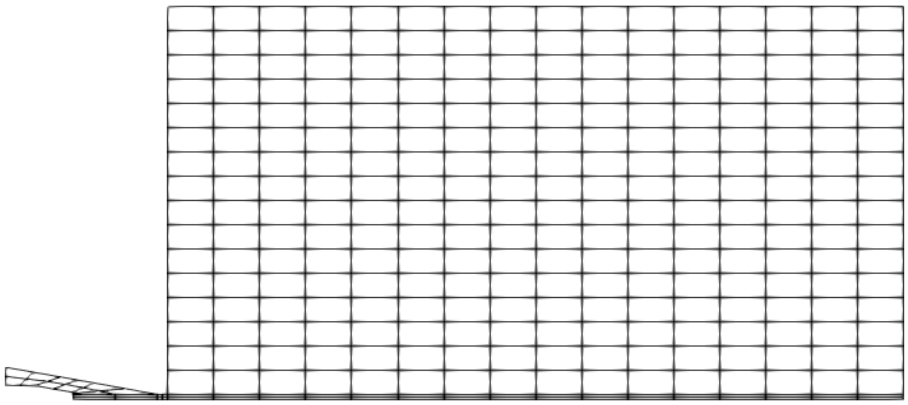

(a) The blocks of the jet simulation.

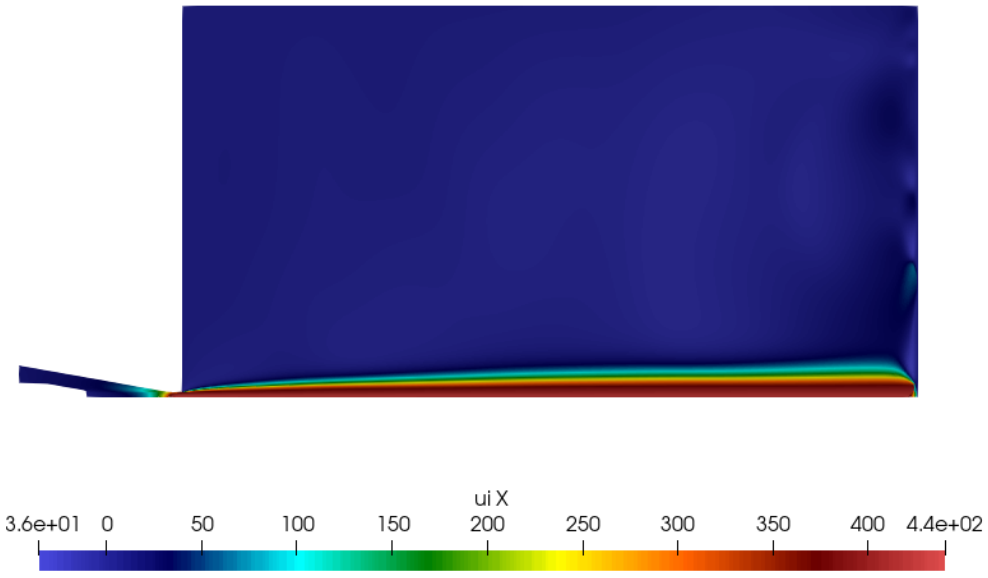

(b) Domain

Figure 4.18: The top image is the mesh of the PWJ, and the bottom is the velocity field in meters per second. This is a PWJ simulation that ran on 308 blocks.

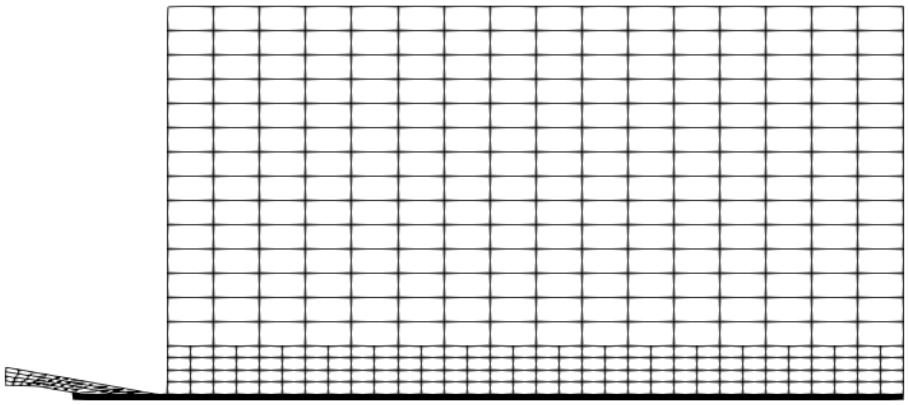

(a) The blocks of the jet simulation.

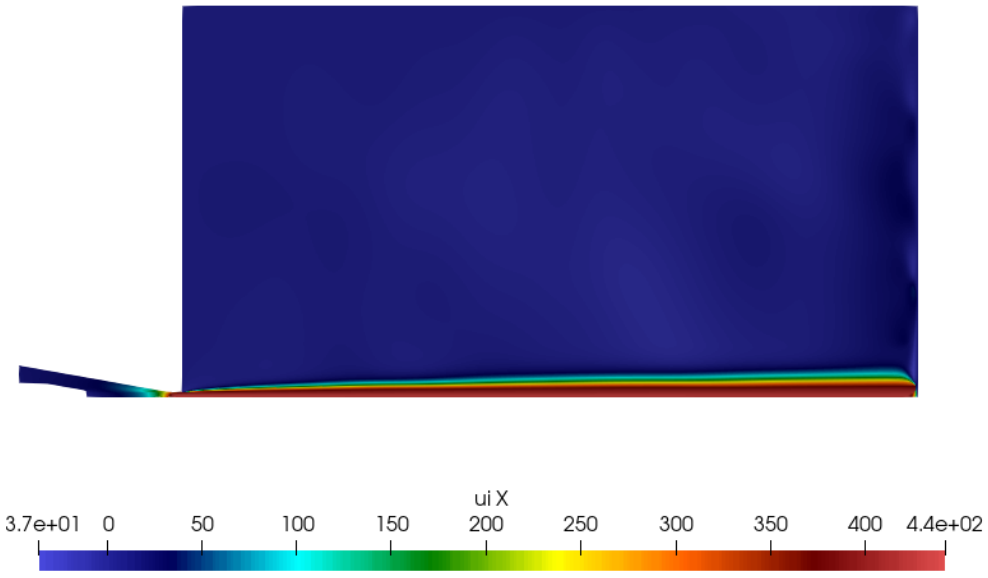

(b) Domain

Figure 4.19: The top image is the mesh of the PWJ, and the bottom is the velocity field in meters per second. This is a PWJ simulation that ran on 554 blocks.

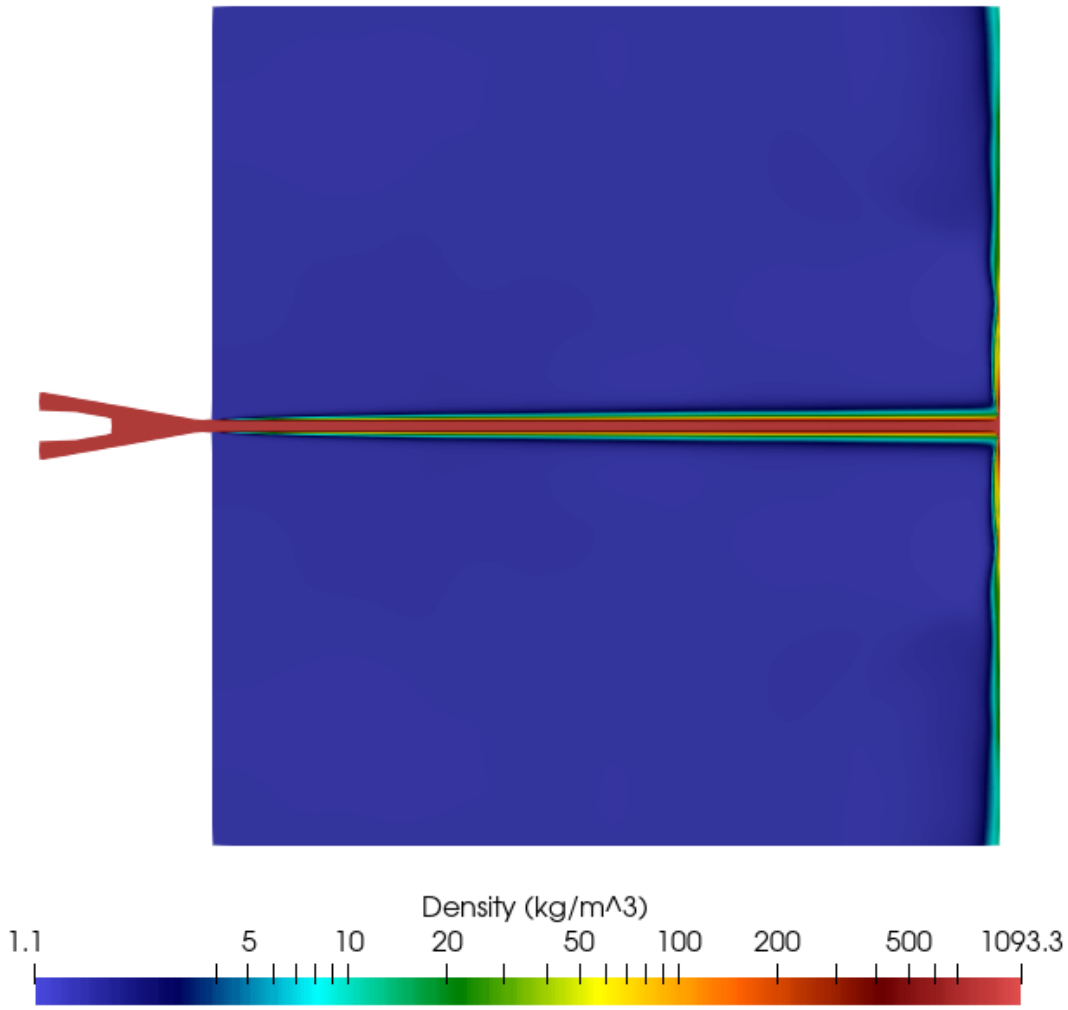

Figure 4.20: Predicted density field of the jet without the oscillatory boundary condition.

hammer effect. The predicted water hammer pressure is 82.6 MPa. This shows that the strength of the jet comes from its speed and the sudden impact against the wall; in Figure 4.22, the top speed of the water jet is 440 m/s. The convergence of the nozzle produces a sharp increase in velocity. As the radius of the jet increases, the velocity also decreases. A final note should be made about the void fraction of vapour, as seen in Figure 4.23; it seems that the geometry of the nozzle causes a vapour bubble to form within the nozzle, which is a phenomenon not created by the oscillating probe.

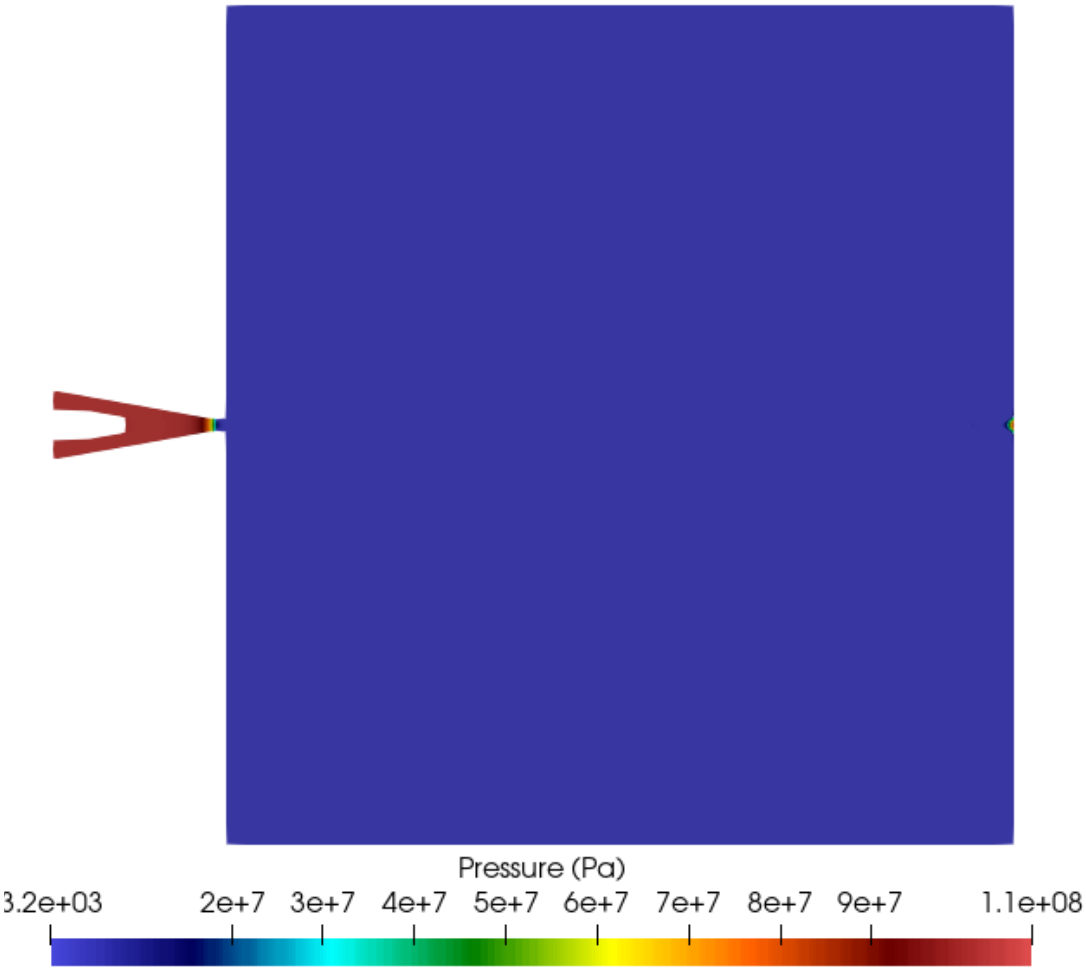

Figure 4.21: Predicted pressure field of the jet without the oscillatory boundary condition.

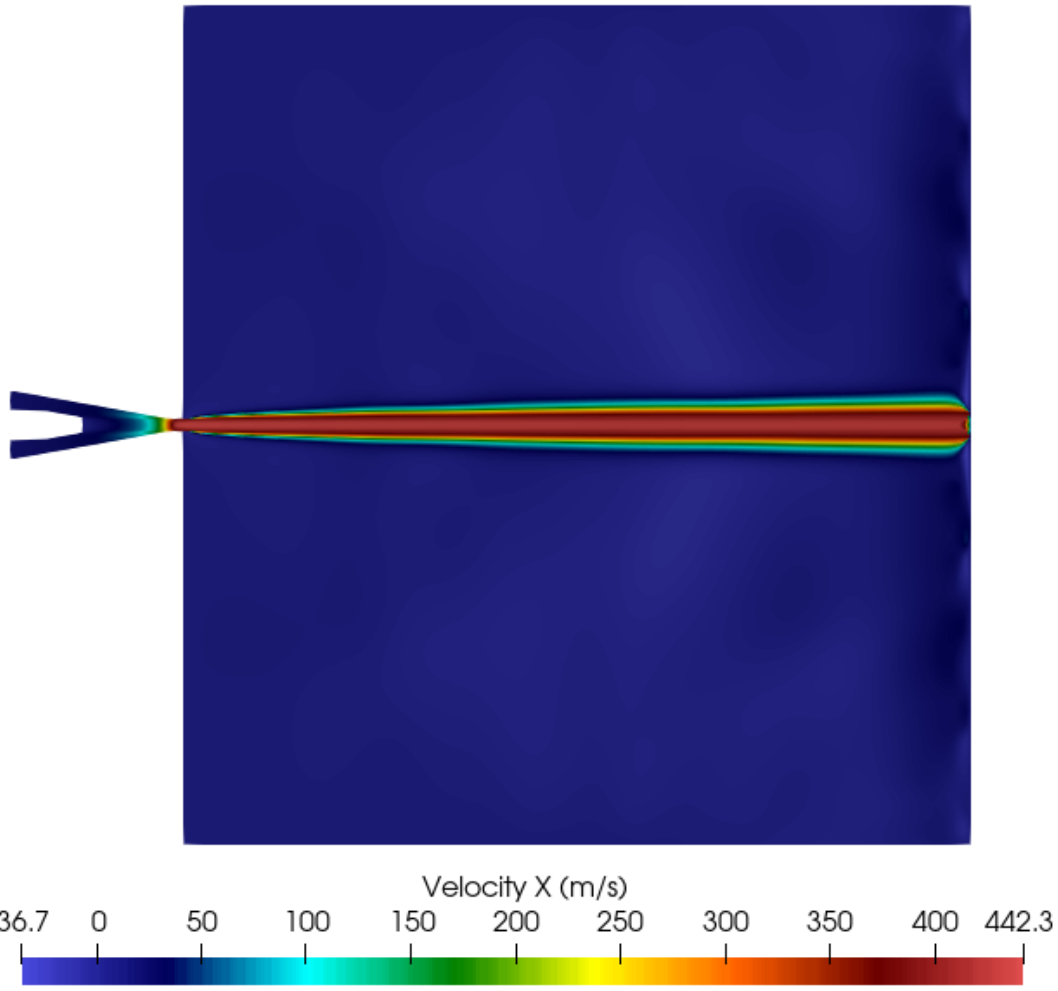

Figure 4.22: The predicted velocity field of the jet without the oscillatory boundary condition.

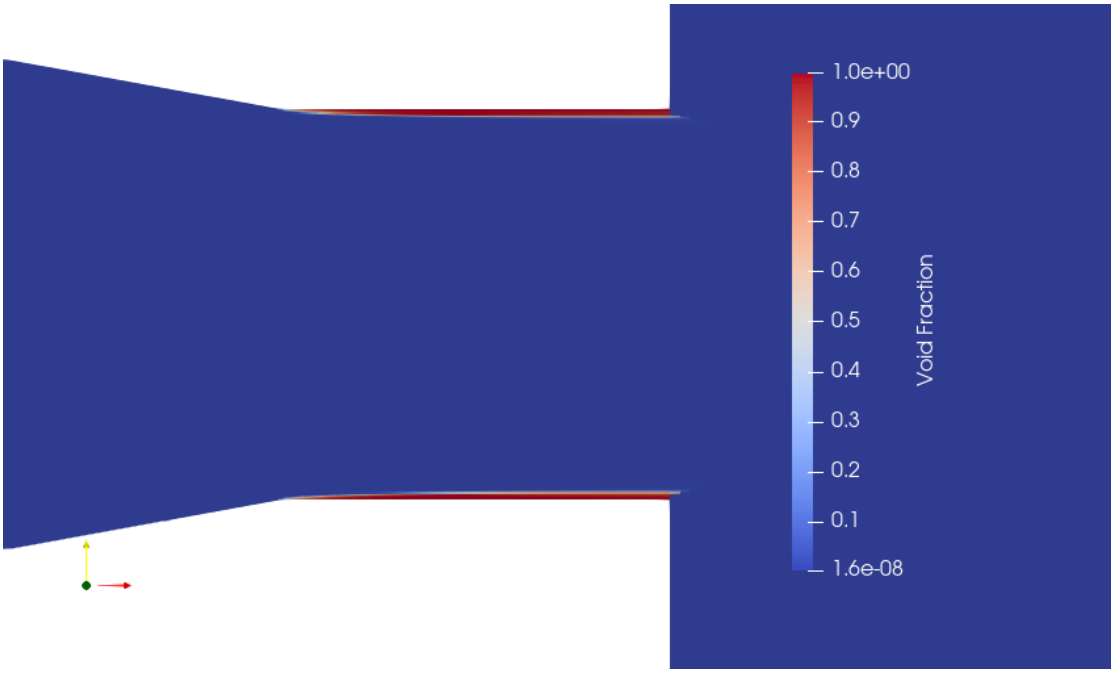

Figure 4.23: The predicted void fraction of the jet without the oscillatory boundary condition.

4.4.3 PWJ with the oscillating boundary condition.

This simulation turns The high-frequency oscillating probe on, and time marched for $t = 0.0058s$. The goal is to show the complex physics in this simulation and how they differ from the jet when the probe is turned off. For this reason, the same mesh used in the PWJ without the probe is used for consistency.

Figure 4.24 shows the density field. The PWJ exhibits the mushroom-like packets described in Vijay et al. study [36]. These mushroom packets occur because of the high-pressure and low-pressure waves created by the oscillating probe. Along the jet, the mushroom packets become larger as the liquid water interacts with the air.

In Figure 4.25, the pressure field is shown, and the pressure waves in the domain with regions of low-pressure waves followed by regions with high-pressure waves can be seen in the water jet. In Figure 4.28, the plot is the water hammer pressure vs time. This plot spans eight oscillations or pulses produced by the oscillating probe. The highest peak creates a pressure of 110 MPa, 23% higher than the standard jet without the oscillating probe. The jet's lowest peak is a

weaker impact of 60 MPa. Therefore, the oscillating probe has more impactful pressure with a repeating pattern versus the standard jet.

The high-speed water jet is even faster with the oscillating probe. In Figure 4.26, the top speed of the water jet is 470 m/s, which is faster than the velocity of the standard jet, which is 440 m/s.

In Figure 4.27 shows pressure field of the water jet in air. In regions of low pressure, the jet seems to have no cavitation bubbles within it as the pressure never comes near the vapour pressure of 2300 Pa. It had been theorized that cavitation forms within the water jet and encourages the creation of discrete water packets that enable the water hammer effect. However, the numerical results do not support this theory.

4.4.4 Conclusion

The simulation demonstrates the oscillating probe's impact on the pulsed waterjet. The PWJ oscillating probe enhances the pressure, velocity, and overall performance.

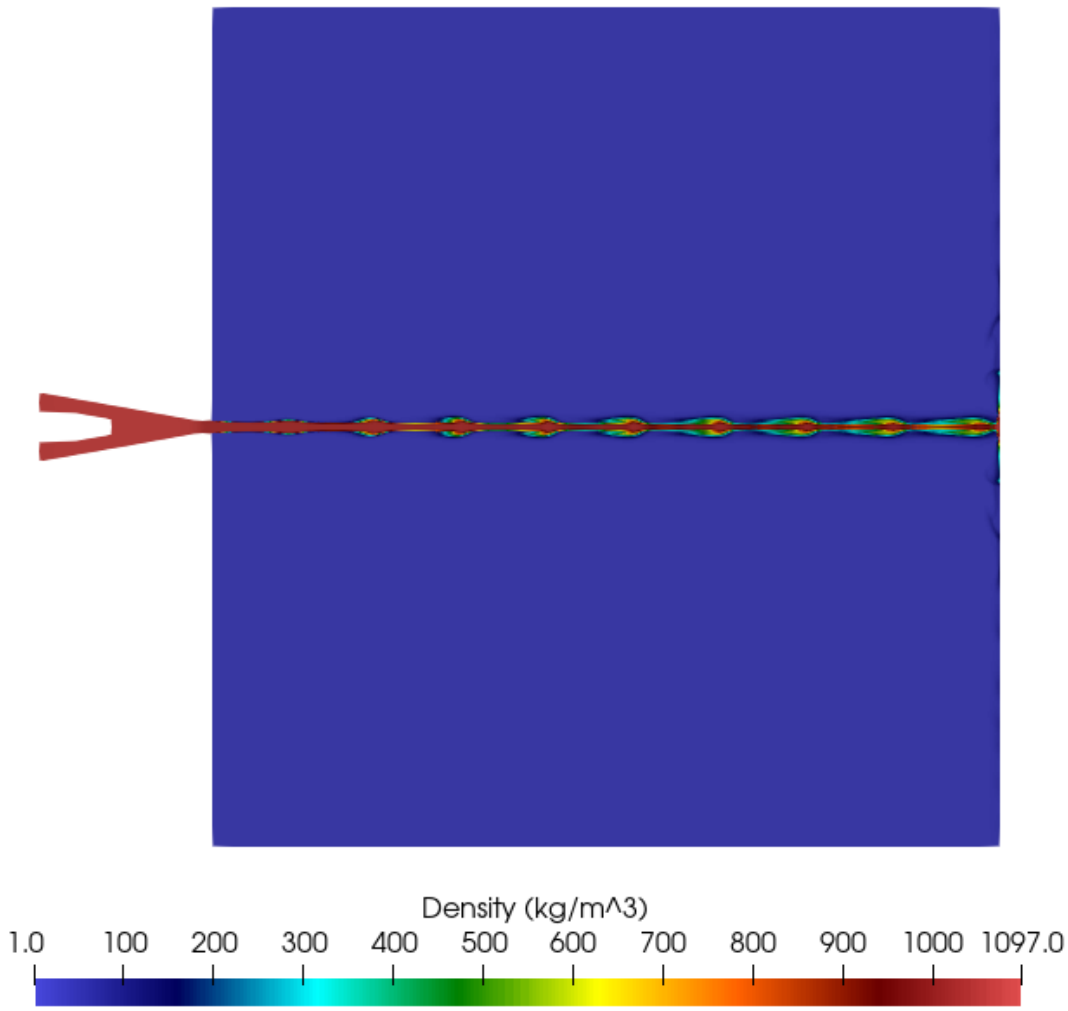

Figure 4.24: The predicted density field of the jet with the oscillating boundary condition.

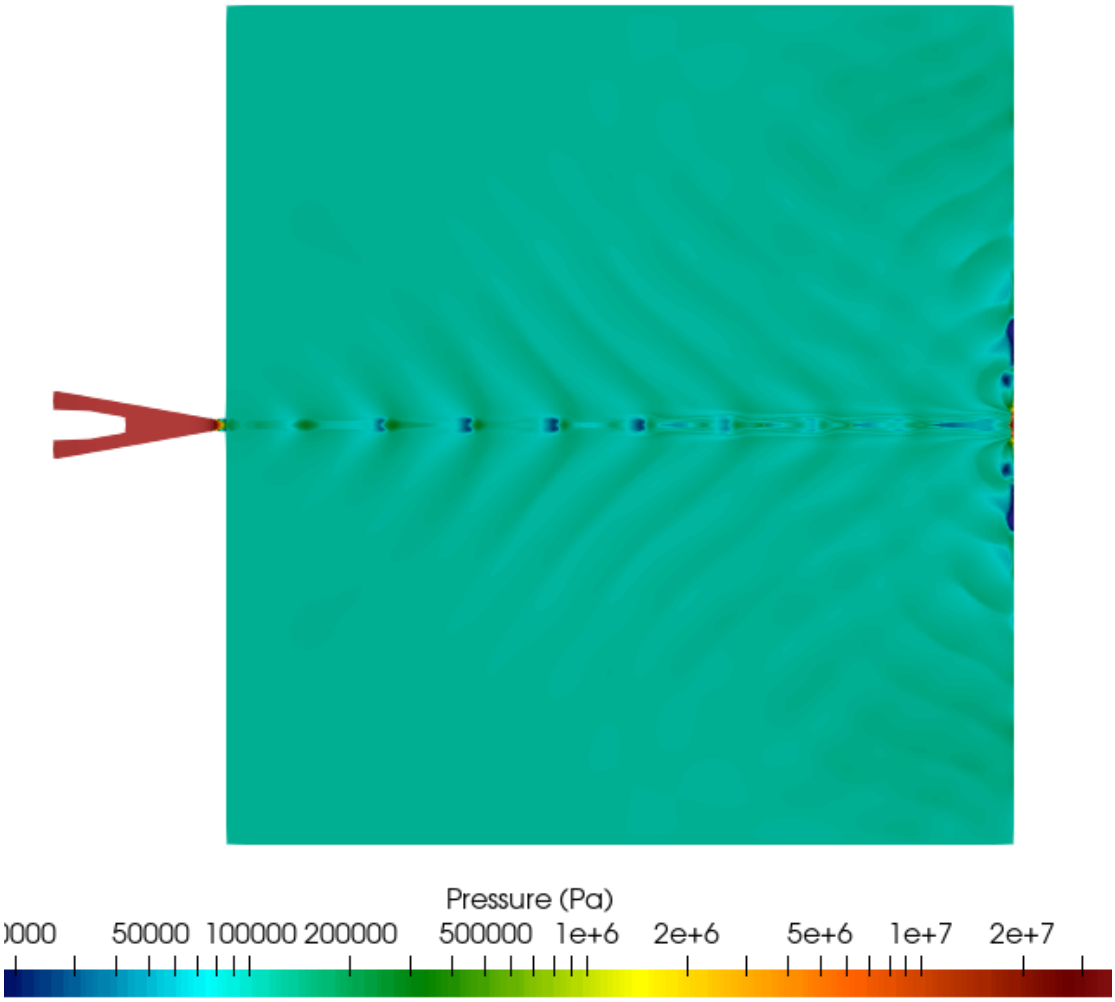

Figure 4.25: The predicted pressure field of the jet with the oscillating boundary condition.

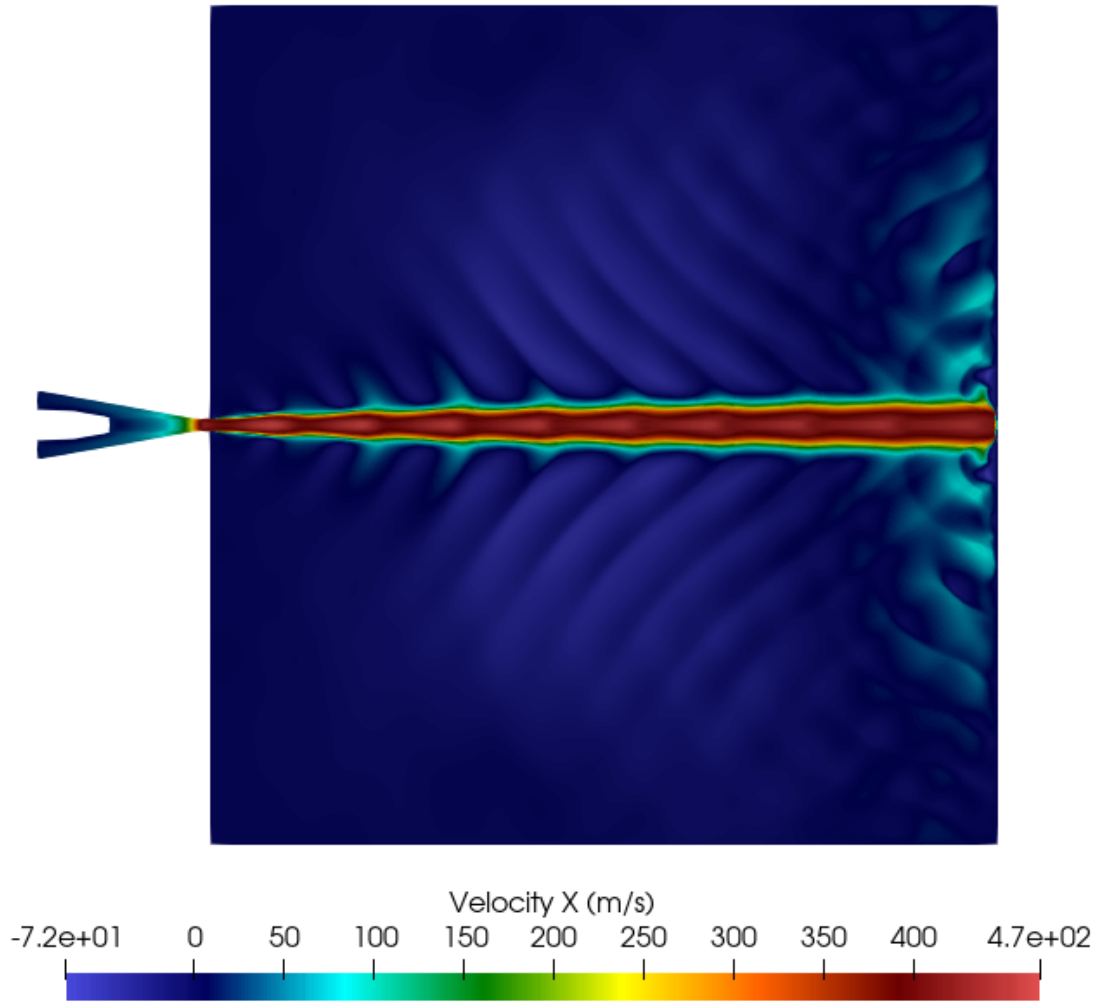

Figure 4.26: The predicted Velocity field with the oscillating boundary condition.

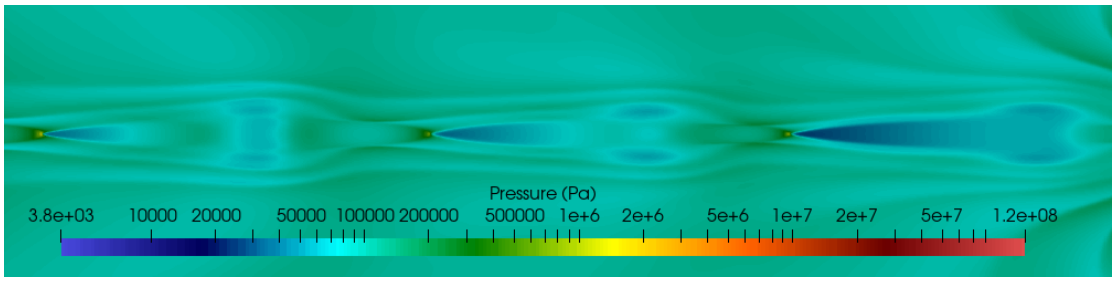

Figure 4.27: The predicted pressure field of the jet with the oscillating boundary condition.

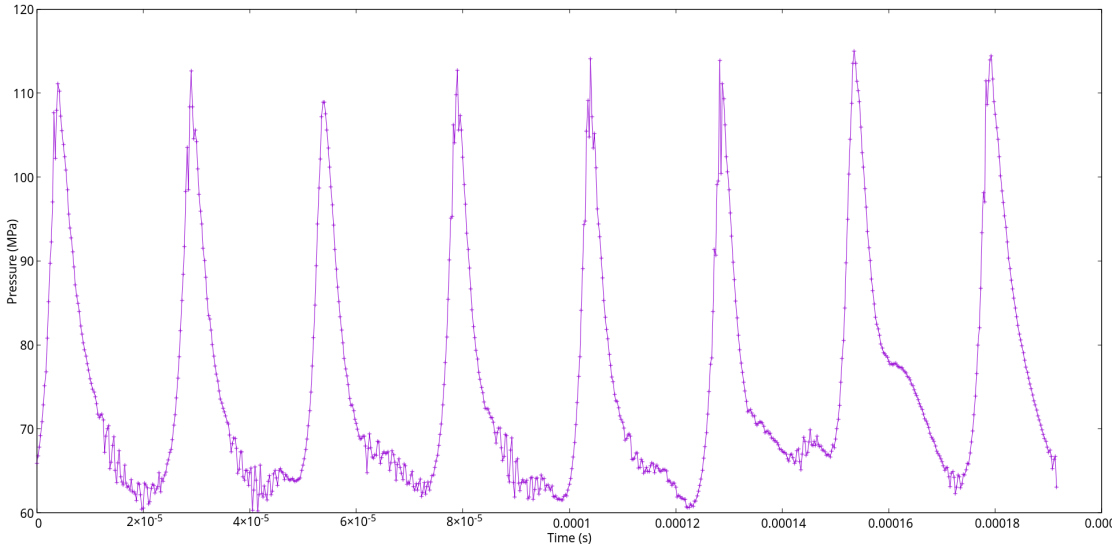

Figure 4.28: A plot of pressure vs time at the point of impact of the jet against the wall.

Chapter 5

Conclusion

The current work presents the use of a phase transition model derived from Saurel's paper [27] for simulating a cavitating venturi nozzle and the pulsed waterjet. The simulations and their results are discussed here. Ultimately, the PWJ jet was successfully simulated with and without the oscillating probe. A suitable phase transition model worked well with the Discontinuous-Galerkin-Hancock method.

One of the main objectives of verifying a phase transition model and equation of state using the Discontinuous-Galerkin-Hancock Method was successful. Classical Riemann problems were solved to verify that the model and numerics were implemented correctly, creating a foundation to accurately model the complex physics within the venturi nozzle and the pulsed waterjet. The venturi nozzle exhibits a quasi-periodic shedding that was successfully simulated by the model and equation of state. This model is also capable of simulating the pulsed waterjet. The oscillating probe improved the jet's operating pressure and velocity. In the simulations, the PWJ jet had cavitation bubbles within the nozzle but had no cavitation bubbles that travelled through the jet. It was theorized that the jet had cavitating bubbles, but the current simulation work does not indicate that this phenomenon occurs.

5.1 Future Work

Regarding improvements to Saurel's model, future work could involve running simulations with varying stiff relaxation parameters, ν. Running the simulations of the venturi nozzle with different stiff relaxation parameters could offer new insights into cavitating flows.

For future work involving the PWJ nozzle, a prospective study could include varying the geometry and operating parameters. This could reveal new insights about the complex flows of the PWJ but could also lead to improvement in the PWJ nozzle design. Another study could involve the variation of the frequency and amplitude parameters of the oscillating probe. This study has shown that the oscillating probe within the PWJ produces a more effective water jet; therefore, studying the effects of frequency and amplitude on the flow is worthwhile.

Bibliography

[1] G. D. van Albada, B. van Leer, and W. W. Roberts. "A Comparative Study of Computational Methods in Cosmic Gas Dynamics". In: *Upwind and High-Resolution Schemes*. Ed. by M. Yousuff Hussaini, Bram van Leer, and John Van Rosendale. Berlin, Heidelberg: Springer Berlin Heidelberg, 1997, pp. 95–103. ISBN: 978-3-642-60543-7. URL: https://doi.org/10.1007/978-3-642-60543-7_6.

[2] S. Barre et al. "Experiments and modeling of cavitating flows in venturi: attached sheet cavitation". In: *European Journal of Mechanics - B/Fluids* 28.3 (2009), pp. 444–464. ISSN: 0997-7546. URL: https://www.sciencedirect.com/science/article/pii/S0997754608000976.

[3] Michel Barret, Eric Faucher, and Jean-Marc Herard. "Schemes to Compute Unsteady Flashing Flows". In: *AIAA Journal* 40.5 (2002), pp. 905–913. eprint: https://doi.org/10.2514/2.1727. URL: https://doi.org/10.2514/2.1727.

[4] Pierre Boivin, M Cannac, and O. Métayer. "A thermodynamic closure for the simulation of multiphase reactive flows". In: *International Journal of Thermal Sciences* 137 (Jan. 2018), pp. 640–649.

[5] John W. Cahn and John E. Hilliard. "Free Energy of a Nonuniform System. I. Interfacial Free Energy". In: *The Journal of Chemical Physics* 28.2 (Aug. 2004), pp. 258–267. ISSN: 0021-9606. eprint: https://pubs.aip.org/aip/jcp/article-pdf/28/2/258/11106115/258_1_online.pdf. URL: https://doi.org/10.1063/1.1744102.

[6] Bernardo Cockburn, Suchung Hou, and Chi-Wang Shu. "The Runge-Kutta Local Projection Discontinuous Galerkin Finite Element Method for Conservation Laws. IV: The Multidimensional Case". In: *Mathematics of Computation* 54.190 (1990), pp. 545–581. ISSN: 00255718, 10886842. URL: http://www.jstor.org/stable/2008501 (visited on 11/17/2022).

[7] P. Downar-Zapolski et al. "The non-equilibrium relaxation model for one-dimensional flashing liquid flow". In: *International Journal of Multiphase Flow* 22.3 (1996), pp. 473–483. ISSN: 0301-9322. URL: https://www.sciencedirect.com/science/article/pii/030193229500078X.

[8] Michael Dumbser and Claus-Dieter Munz. "ADER discontinuous Galerkin schemes for aeroacoustics". In: *Comptes Rendus Mécanique* 333.9 (2005). Computational AeroAcoustics: from acoustic sources modeling to farfield radiated noise prediction, pp. 683–687. ISSN: 1631-0721. URL: https://www.sciencedirect.com/science/article/pii/S1631072105001191.

[9] Michael Dumbser and Claus-Dieter Munz. "Building Blocks for Arbitrary High Order Discontinuous Galerkin Schemes". In: *J. Sci. Comput.* 27 (June 2006), pp. 215–230.

[10] Josef Foldyna. "Use of Acoustic Waves for Pulsating Water Jet Generation". In: *Acoustic Waves*. Ed. by Marco G. Beghi. Rijeka: IntechOpen, 2011. Chap. 15. URL: https://doi.org/10.5772/18862.

[11] Regiane . Fortes Patella, Stéphane Barre, and Jean-Luc Reboud. "Experiments and modelling of cavitating flows in Venturi. Part II: unsteady cavitation". In: *CAV 2006 Symposium*. Wageningen, Netherlands, Sept. 2006. URL: https://hal.science/hal-00212023.

[12] Damien Furfaro et al. "Towards sodium combustion modeling with liquid water". In: *Journal of Computational Physics* 403 (2020), p. 109060. URL: https://doi.org/10.1016%2Fj.jcp.2019.109060.

[13] J.J Gottlieb and C.P.T Groth. "Assessment of riemann solvers for unsteady one-dimensional inviscid flows of perfect gases". In: *Journal of Computational Physics* 78.2 (1988), pp. 437–458. ISSN: 0021-9991. URL: https://www.sciencedirect.com/science/article/pii/0021999188900599.

[14] Ami Harten. "High resolution schemes for hyperbolic conservation laws". In: *Journal of Computational Physics* 49.3 (1983), pp. 357–393. ISSN: 0021-9991. URL: https://www.sciencedirect.com/science/article/pii/0021999183901365.

[15] H. T. Huynh. "An Upwind Moment Scheme for Conservation Laws". In: *Computational Fluid Dynamics 2004*. Ed. by Clinton Groth and David W. Zingg. Berlin, Heidelberg: Springer Berlin Heidelberg, 2006, pp. 761–766. ISBN: 978-3-540-31801-9.

[16] C. Johnson and J. Pitkäranta. "An Analysis of the Discontinuous Galerkin Method for a Scalar Hyperbolic Equation". In: *Mathematics of Computation* 46.173 (1986), pp. 1–26. ISSN: 00255718, 10886842. URL: http://www.jstor.org/stable/2008211 (visited on 11/17/2022).

[17] Peter Lax and Burton Wendroff. "Difference Schemes for Hyperbolic Equations with High Order of Accuracy". In: *Communications on Pure and Applied Mathematics - COMMUN PURE APPL MATH* 17 (2005), pp. 284–301.

[18] O Le Métayer and Richard Saurel. "The Noble-Abel Stiffened-Gas equation of state". In: *Physics of Fluids* 28 (2016), p. 046102. URL: https://hal.science/hal-01305974.

[19] P. Lesaint and P. A. Raviart. "On a Finite Element Method for Solving the Neutron Transport Equation". en. In: *Publications des séminaires de mathématiques et informatique de Rennes* S4, 8 (1974). URL: http://www.numdam.org/item/PSMIR_1974___S4_A8_0/.

[20] E. B. Nebeker and S. E. Rodriguez. *Percussive Water Jets for Rapid Excavation*. Tech. rep. Final Report; Contract No DAA K 02-73-C-0163. Fort Belvoir, VA, USA: US Army Mobility Equipment, 1973.

[21] E. B. Nebeker and S. E. Rodriguez. "Percussive water jets for rock cutting". In: *Proceedings of the 3rd International Symposium on Jet Cutting Technology*. Chicago, IL, USA, May 11, 1976, B1:1–B1:9.

[22] Izaak Neutelings. *Phase transitions*. https://tikz.net/phase_transitions/. Accessed: December 29, 2023. 2021.

[23] Todd E. Peterson. "A Note on the Convergence of the Discontinuous Galerkin Method for a Scalar Hyperbolic Equation". In: *SIAM Journal on Numerical Analysis* 28.1 (1991), pp. 133–140. eprint: https://doi.org/10.1137/0728006. URL: https://doi.org/10.1137/0728006.

[24] Matei Ioan Radulescu. *Compressible flow in a Noble-Abel Stiffened-Gas fluid*. 2020. arXiv: 2004.08750 [physics.flu-dyn].

[25] W H Reed and T R Hill. "Triangular mesh methods for the neutron transport equation". In: *Proceedings of the American Nuclear Society*. Oct. 1973. URL: https://www.osti.gov/biblio/4491151.

[26] Tajwar Samson et al. "Effect of Pulsed Waterjet Surface Preparation on the Adhesion Strength of Cold Gas Dynamic Sprayed Aluminum Coatings". In: *Journal of Thermal Spray Technology* 24 (July 2015), pp. 984–993.

[27] Richard Saurel, Pierre Boivin, and Olivier Métayer. "A general formulation for cavitating, boiling and evaporating flows". In: *Computers & Fluids* 128 (Jan. 2016).

[28] Richard Saurel and Loann Neron. *Noble-Abel / First-order virial equations of state for gas mixtures resulting of multiple condensed reactive materials combustion*. 2021. arXiv: 2111.10120 [math.AP].

[29] W. E. Schiesser. "The Numerical Method of Lines: Integration of Partial Differential Equations". In: *Mathematics of Computation* 60.201 (1993), pp. 433–437. ISSN: 00255718, 10886842. URL: http://www.jstor.org/stable/2153182 (visited on 12/29/2023).

[30] Yoshifumi Suzuki and Bram van Leer. "A Space-Time Discontinuous Galerkin Method for Extended Hydrodynamics". In: Nov. 2010, pp. 245–302. ISBN: 978-88-548-3360-9.

[31] A. Tieu et al. *Feasibility study of decontaminating steel ducts and pipes for decommissioning nuclear facilities with Forced Pulsed Water Jetting (FPWJ).* http://www.vln-tech.com/pdf_uploads/BHR-Water-JettingConference-2016-Alex-Jenkins-Surface-Prep.pdf. Accessed: December 29, 2023. 2016.

[32] E. F. Toro, R. C. Millington, and L. A. M. Nejad. "Towards Very High Order Godunov Schemes". In: *Godunov Methods: Theory and Applications*. Ed. by E. F. Toro. New York, NY: Springer US, 2001, pp. 907–940. ISBN: 978-1-4615-0663-8. URL: https://doi.org/10.1007/978-1-4615-0663-8_87.

[33] Bram Van Leer. "Towards the ultimate conservative difference scheme. IV. A new approach to numerical convection". In: *Journal of Computational Physics* 23.3 (1977), pp. 276–299. ISSN: 0021-9991. URL: https://www.sciencedirect.com/science/article/pii/002199917790095X.

[34] V. Venkatakrishnan. "Convergence to Steady State Solutions of the Euler Equations on Unstructured Grids with Limiters". In: *Journal of Computational Physics* 118.1 (1995), pp. 120–130. ISSN: 0021-9991. URL: https://www.sciencedirect.com/science/article/pii/S0021999185710844.

[35] M. M. Vijay, J. Foldyna, and J. Remisz. "Ultrasonic modulation of high-speed water jets". In: *Geomechanics 93*. Vol. 1. CRC Press, 1994, pp. 327–332.

[36] M. M. Vijay, M. K. Y. Lai, and M. Jiang. “Computational Fluid Dynamic Analysis and Visualization of High Frequency Pulsed Water Jets”. In: *Proc. 8th American Waterjet Conference*. WJTA. St. Louis, USA, 1995, pp. 557–572.

[37] A. B. (Albert Beaumont) Wood. *A textbook of sound : being an account of the physics of vibrations with special reference to recent theoretical and technical developments*. eng. New York: The Macmillan company, 1941.